Improved effective-one-body model of spinning, nonprecessing binary black holes for the era of gravitational-wave astrophysics with advanced detectors

Alejandro Bohé,[1,*] Lijing Shao,[1,†] Andrea Taracchini,[1,‡] Alessandra Buonanno,[1,2] Stanislav Babak,[1] Ian W. Harry,[1] Ian Hinder,[1] Serguei Ossokine,[1] Michael Pürrer,[1] Vivien Raymond,[1] Tony Chu,[3,4] Heather Fong,[4,5] Prayush Kumar,[4] Harald P. Pfeiffer,[4,1,6] Michael Boyle,[7] Daniel A. Hemberger,[8] Lawrence E. Kidder,[7] Geoffrey Lovelace,[10] Mark A. Scheel,[8] and Béla Szilágyi[8,9]

[1]*Max Planck Institute for Gravitational Physics (Albert Einstein Institute), Am Mühlenberg 1, Potsdam 14476, Germany*
[2]*Department of Physics, University of Maryland, College Park, Maryland 20742, USA*
[3]*Department of Physics, Princeton University, Jadwin Hall, Princeton, New Jersey 08544, USA*
[4]*Canadian Institute for Theoretical Astrophysics, University of Toronto, Toronto M5S 3H8, Canada*
[5]*Department of Physics, University of Toronto, Toronto M5S 3H8, Canada*
[6]*Canadian Institute for Advanced Research, Toronto M5G 1Z8, Canada*
[7]*Cornell Center for Astrophysics and Planetary Science, Cornell University, Ithaca, New York, 14853, USA*
[8]*Theoretical Astrophysics 350-17, California Institute of Technology, Pasadena, California 91125, USA*
[9]*Jet Propulsion Laboratory, California Institute of Technology, 4800 Oak Grove Drive, Pasadena, California 91109, USA*
[10]*Gravitational Wave Physics and Astronomy Center, California State University Fullerton, Fullerton, California 92834, USA*

(Received 14 November 2016; published 17 February 2017)

We improve the accuracy of the effective-one-body (EOB) waveforms that were employed during the first observing run of Advanced LIGO for binaries of spinning, nonprecessing black holes by calibrating them to a set of 141 numerical-relativity (NR) waveforms. The NR simulations expand the domain of calibration toward larger mass ratios and spins, as compared to the previous EOBNR model. Merger-ringdown waveforms computed in black-hole perturbation theory for Kerr spins close to extremal provide additional inputs to the calibration. For the inspiral-plunge phase, we use a Markov-chain Monte Carlo algorithm to efficiently explore the calibration space. For the merger-ringdown phase, we fit the NR signals with phenomenological formulae. After extrapolation of the calibrated model to arbitrary mass ratios and spins, the (dominant-mode) EOBNR waveforms have faithfulness—at design Advanced-LIGO sensitivity—above 99% against all the NR waveforms, including 16 additional waveforms used for validation, when maximizing only on initial phase and time. This implies a negligible loss in event rate due to modeling for these binary configurations. We find that future NR simulations at mass ratios $\gtrsim 4$ and double spin $\gtrsim 0.8$ will be crucial to resolving discrepancies between different ways of extrapolating waveform models. We also find that some of the NR simulations that already exist in such region of parameter space are too short to constrain the low-frequency portion of the models. Finally, we build a reduced-order version of the EOBNR model to speed up waveform generation by orders of magnitude, thus enabling intensive data-analysis applications during the upcoming observation runs of Advanced LIGO.

DOI: 10.1103/PhysRevD.95.044028

I. INTRODUCTION

During its first observing run (O1), the Advanced Laser Interferometer Gravitational wave Observatory (LIGO) detected gravitational waves (GWs) emitted by the coalescence of two binary black holes (BBHs), GW150914 and GW151226 [1,2]. A third candidate event, LVT151012, was also recorded [3], but with not high enough statistical significance to claim a detection. These discoveries opened the possibility of observing and probing the most extreme astrophysical objects in the Universe.

GW150914 was a loud event, detected with a signal-to-noise ratio (SNR) of ∼24. It was initially identified by an (online) generic-transient search [4], which uses minimal assumptions about waveforms. The highest statistical confidence was obtained with the (offline) optimal matched-filtering searches [4] that employ waveforms predicted by general relativity. By contrast, matched-filtering searches were essential for detecting GW151226 [2,3], which was an event quieter than GW150914, having a SNR of ∼13 and an energy spread over about 1 sec (∼55 GW cycles), instead of 0.2 sec (∼10 GW cycles).

*alejandro.bohe@aei.mpg.de
†lijing.shao@aei.mpg.de
‡andrea.taracchini@aei.mpg.de

During the O1 run, the Advanced-LIGO matched-filtering search targeted GWs from binary systems with component masses between 1 $M_\odot$ and 99 $M_\odot$, total mass smaller than 100 $M_\odot$, and dimensionless aligned-spin magnitudes up to 0.99. For total masses larger than 4 $M_\odot$, it used a template bank [3,5,6] of ∼250,000 (semianalytical) spinning, nonprecessing templates developed in Refs. [7,8] within the effective-one-body (EOB) formalism. This analytical approach, which describes the dynamics of coalescing BBHs and the associated gravitational radiation, was originally developed in the late 1990s [9,10] and over the years it has been further improved [7,11–26]. In particular, newly available results from perturbative approaches to the two-body problem in general relativity (GR) (post-Newtonian expansion, BH perturbation theory, and gravitational self-force formalism), as well as crucial nonperturbative information accessible only through numerical relativity (NR) have been incorporated into the framework, gradually extending the region in parameter space over which the model provides highly accurate predictions for inspiral, merger, and ringdown gravitational waveforms. As a result, since the first LIGO search for BBHs in 2005 [27], EOBNR waveforms have been employed in LIGO/Virgo data analyses, and, as discussed above, have played a central role in the detection [2], and subsequent parameter-estimation analyses [3,28,29] and GR tests [3,30] of the GW observations announced earlier this year. EOB waveform models have also been employed to build frequency-domain, phenomenological models [31,32] for the inspiral, merger, and ringdown stages of the BBH coalescence. Those models [33,34] have also been used to infer the properties and carry out tests of GR with GW150914 and GW151226 [3,28,30].

In this paper, we build an improved version of SEOBNRv2 [7,8], the spinning, nonprecessing EOBNR waveform model that was used for O1, and whose accuracy was recently found to degrade [35] in some regions of the BBH parameter space, notably large aligned spins and unequal masses, where the model was extrapolating away from the NR waveforms that were available at the time of its calibration. The improvements developed in this paper include: (i) the addition of all 4PN terms to the EOB radial potential and of higher-order PN corrections to the polarization modes, (ii) a recalibration of the EOB model to a large set of recently produced NR waveforms, which expand the domain of calibration towards larger mass ratios and aligned-spin components, and (iii) a more robust description of the merger-ringdown signal. The updated EOBNR model (SEOBNRv4) has been coded in the LIGO Algorithm Library (LAL) [36], so that it can be employed during the second observing (O2) run of Advanced LIGO, which is scheduled to start later this year, and later runs, enhancing our ability to extract physical information and interpret future GW detections.

The paper is organized as follows. In Sec. II we discuss the EOBNR model of spinning, nonprecessing BBHs, emphasizing the new ingredients with respect to the previous model [7]. In Sec. III we review the catalog of NR simulations and BH perturbation-theory waveforms that we use to calibrate the model. In Sec. IV we describe how to tune the inspiral-plunge calibration parameters to NR simulations using a newly developed Markov-chain Monte Carlo code. We discuss the performance of the model after interpolating and extrapolating it to the entire parameter space, and in Sec. V we compare it to previously developed spinning, nonprecessing waveform models. In Sec. VI we highlight how short NR simulations cannot constrain the low-frequency portion of waveform models. Section VII describes the reduced-order version of the EOBNR model, which is used to speed up the waveform generation, allowing its application in Advanced LIGO and Virgo data analyses. In Sec. VIII we provide our concluding remarks. In Appendix A we summarize information on the NR (dominant-mode) waveforms around the time of merger, which are also included in the EOBNR model. Finally, Appendix B provides fitting formulas for constructing the merger-ringdown signal of the EOBNR model.

Henceforth, we adopt geometric units: $G = 1 = c$.

II. MOTIVATION AND OVERVIEW OF THE EFFECTIVE-ONE-BODY FORMALISM

The problem of describing the GW signal generated by a pair of BHs that (quasicircularly) orbit each other and eventually merge into a single BH is challenging because of the different dynamical regimes that this process spans. When the binary is wide—say, as compared to the BH horizons—the component objects move at orbital speeds (in the center-of-mass frame) that are small with respect to the speed of light. During this phase of the coalescence, the post-Newtonian (PN) (i.e., slow-motion and weak-field) approximation to general relativity can be employed to model the orbital dynamics and the associated GW emission (see., e.g., Ref. [37] for an extensive review of the current status of PN theory applied to the two-body problem). As the BHs spiral in, plunge and eventually merge, their orbital motion becomes more relativistic and the GW energy flux is stronger. NR techniques are required to obtain highly-accurate waveforms during this stage of the process. State-of-the-art codes can now accurately evolve BBHs for several tens of orbits (∼40–60) in large regions of the parameter space [38–42]: (i) at large mass ratios (∼8), but for moderate BH (dimensionless) spin magnitudes (∼0.6), and (ii) at higher BH spin magnitudes, but for comparable masses (∼1–3). Shorter simulations (∼10) can also be produced for mass ratios ∼20 and spin magnitudes ∼0.8. The longest NR run to date covers 175 orbits of a non-spinning BBH with mass ratio 7 [43]. Finally, soon after the merger, a distorted remnant BH is born. This relaxes into a stationary Kerr spacetime by radiating GWs that are well described by BH perturbation theory, as well as by NR.

In spite of tremendous progress, a purely NR approach to simulating BBHs for any possible configuration down to

the lower edge of the sensitive frequency band of current ground-based GW detectors is not feasible yet. This motivated the need to develop more sophisticated semi-analytical waveform models [7,8,26,33,34,44] that, while being cheap to compute for data analysis, are very good approximations to general relativity.

In this section we review the main features of the EOB approach for spinning, nonprecessing binary BHs and describe the improvements that we introduce with respect to the previous EOBNR model [7,45], which was employed during the O1 data analyses.

A. Conservative dynamics

The EOB formalism aims at combining all available results that describe the general-relativistic two-body problem—both analytical and numerical—into a unified description. In the case of a binary composed of BHs, let $m_{1,2}$ and $\boldsymbol{S}_{1,2}$ be the masses and spins of the two component objects as used in the PN description of the *real problem*. Let $q \equiv m_1/m_2 \geq 1$ be the mass ratio of the binary. The key ingredient of the EOB model is a resummation of the conservative PN dynamics of a generic BBH in terms of the conservative dynamics of a test particle with mass μ and spin $\boldsymbol{S}_*$ in a deformed Kerr metric with mass M and spin $\boldsymbol{S}_{\rm Kerr}$ (*effective problem*), the deformation parameter being μ/M. In analogy with the Newtonian treatment of a self-gravitating binary, here μ is the reduced mass of the BBH, while M is its total mass. As to the spins $\boldsymbol{S}_*$ and $\boldsymbol{S}_{\rm Kerr}$, these are given as functions of $m_{1,2}$, $\boldsymbol{S}_{1,2}$ and the dynamical variables. These relationships between mass and spin parameters of the real and effective problem are obtained imposing (i) a precise energy mapping between the two systems, and (ii) requiring that the Hamiltonian describing the effective problem reduces to that of the real problem in the slow-motion, weak-field limit. In particular, the *energy mapping* prescribes that [9]

$$H_{\rm EOB} = M\sqrt{1+2\nu\left(\frac{H_{\rm eff}}{\mu}-1\right)} - M, \tag{2.1}$$

where $\nu \equiv \mu/M$ is the symmetric mass ratio of the real system, $H_{\rm EOB}$ is the EOB resummed Hamiltonian for the real problem and $H_{\rm eff}$ is the Hamiltonian for the effective problem. The explicit form of $H_{\rm EOB}$ that we shall adopt in this paper was derived in Refs. [18,46], based on the linear-in-spin Hamiltonian for spinning test particles of Ref. [17]. When PN-expanded, the EOB Hamiltonian that we employ in this paper reproduces: (i) spin-spin couplings at leading order for any mass ratio, (ii) spin-orbit couplings up to next-to-next-to-leading order for any mass ratio, and (iii) all spin-orbit couplings in the test-particle limit.

We describe the EOB orbital dynamics in terms of the following quantities: the (dimensionless) radial separation r (in units of M), the orbital phase ϕ, and their conjugate (dimensionless) momenta, p_r and p_ϕ (in units of μ). Of course, since we consider only spins that are aligned or antialigned with the orbital angular momentum, their projections on $\hat{\boldsymbol{L}}_N$ (with $\hat{\boldsymbol{L}}_N$ being the direction of the Newtonian angular momentum) are constant; we denote them via $\chi_{1,2} \equiv (\boldsymbol{S}_{1,2}\cdot\hat{\boldsymbol{L}}_N)/m_{1,2}^2$. Note that $-1 \leq \chi_{1,2} \leq 1$.

The effective Hamiltonian depends on a radial potential that enters the 00-component of the effective deformed metric, it reads [7,45]

$$\Delta_u = \chi_{\rm Kerr}^2\left(u-\frac{1}{r_+^{\rm EOB}}\right)\left(u-\frac{1}{r_-^{\rm EOB}}\right) \times\left[1+\nu\Delta_0+\log\left(1+\sum_{i=1}^{5}\frac{\Delta_i}{r^i}\right)\right], \tag{2.2}$$

where $\chi_{\rm Kerr} \equiv (\boldsymbol{S}_{\rm Kerr}\cdot\hat{\boldsymbol{L}}_N)/M^2$, u is the inverse of the EOB radial coordinate, $r_\pm^{\rm EOB} \equiv (1-\nu K)[1\pm(1-\chi_{\rm Kerr}^2)^{1/2}]$ (with K a calibration parameter). We observe that Δ_u vanishes at the EOB horizon $r = r_+^{\rm EOB}$. The Δ_i's used in the previous version of the spinning, nonprecessing EOBNR model [7,45] can be found in Appendix A of Ref. [47]. Here, we augment the 4PN coefficient Δ_5 by the quadratic-in-ν corrections that were computed in Ref. [48]

$$\Delta_5 \supset (1-\nu K)^2\left(\frac{41\pi^2}{32}-\frac{221}{6}\right)\nu. \tag{2.3}$$

We adopt the same mapping between the spin variables in the real and effective descriptions of Refs. [7,45], and include the same spin-orbit and spin-spin calibration parameters, $d_{\rm SO}$ and $d_{\rm SS}$.

B. Inspiral-plunge waveforms and dissipative dynamics

The conservative dynamics described above is complemented by analytic formulas for the inspiral-plunge GW multipolar modes $h_{\ell m}^{\rm insp\text{-}plunge}$. These expressions are a recasting of PN results [49,50] into a factorized form [15,19,51] that is meant to capture strong-field features that are observed when numerically computing the gravitational perturbations of isolated Kerr BHs by test particles on circular, equatorial orbits down to the innermost stable circular orbit (ISCO). The factorized formulas are functions of the EOB orbital dynamics. Here, we adopt the same expressions that were used in Ref. [7] with the addition of new amplitude corrections to the (2,2) mode that enter the ρ_{22} factor (see Ref. [19]) at 2.5PN order, that is

$$\left[\left(-\frac{34}{21}+\frac{49\nu}{18}+\frac{209\nu^2}{126}\right)\chi_{\rm S}-\left(\frac{34}{21}+\frac{19\nu}{42}\right)\chi_{\rm A}\delta\right]v_\Omega^5, \tag{2.4}$$

and at 3.5PN order, that is

$$\left[\left(\frac{18733}{15876}+\frac{74749\nu}{5292}-\frac{245717\nu^2}{63504}+\frac{50803\nu^3}{63504}\right)\chi_{\rm S} +\left(\frac{18733}{15876}+\frac{50140\nu}{3969}+\frac{97865\nu^2}{63504}\right)\chi_{\rm A}\delta\right]v_\Omega^7, \tag{2.5}$$

as well as new phase corrections that enter the δ_{22} factor (again, see Ref. [19]) at 3PN order, that is

$$-\frac{4}{3}[\chi_{\rm S}(1-2\nu)+\chi_{\rm A}\delta](\Omega H_{\rm EOB})^2. \tag{2.6}$$

Here $\chi_{\rm S,A}\equiv(\chi_1\pm\chi_2)/2$, $\delta\equiv(m_1-m_2)/M$, and $v_\Omega\equiv(M\Omega)^{1/3}$, where $\Omega\equiv {\rm d}\phi/{\rm d}t$ is the orbital frequency. Note that the amplitude corrections in Eqs. (2.4)–(2.5) replace the spinning test-particle-limit terms that were used in Ref. [7] at those PN orders. The 2.5PN correction (2.4) to the factorized waveform was derived in Ref. [52]. We derived the ones in the phase at 3PN order and in the amplitude at 3.5PN order [Eqs. (2.6) and (2.5), respectively] for this paper starting from the Taylor expanded PN results of Refs. [53,54], respectively.

Like in previous EOBNR models, we apply nonquasicircular (NQC) corrections to the (2,2) mode with the aim of describing the NR merger signals at and around the peak of GW emission in the most accurate way. In particular, we multiply the factorized formula for the (2,2) mode by [7,45]

$$N_{22}=\left[1+\left(\frac{p_{r^*}}{rM\Omega}\right)^2\left(a_1^{h_{22}}+\frac{a_2^{h_{22}}}{r}+\frac{a_3^{h_{22}}}{r^{3/2}}\right)\right]\times\exp\left[\frac{ip_{r^*}}{rM\Omega}(b_1^{h_{22}}+b_2^{h_{22}}p_{r^*}^2)\right], \tag{2.7}$$

where p_{r^*} is the conjugate momentum to the tortoise coordinate r^* (see Ref. [55]), and the coefficients $a_i^{h_{22}}$ $(i=1,2,3)$ and $b_i^{h_{22}}$ $(i=1,2)$ are fixed by imposing that amplitude, curvature of the amplitude, GW frequency, and slope of the GW frequency match fits of such quantities (often referred to as "input values") to NR data. This amounts to solving 2 linear systems of equations, one for the $a_i^{h_{22}}$'s $(i=1,2,3)$ and one for the $b_i^{h_{22}}$'s. In the model, the input values are enforced at a time $t^{22}_{\rm peak}\equiv t^{\Omega}_{\rm peak}+\Delta t^{22}_{\rm peak}$, where $t^{\Omega}_{\rm peak}$ is the time when the peak of Ω occurs and $\Delta t^{22}_{\rm peak}$ is a calibration parameter. The introduction of the time lag $\Delta t^{22}_{\rm peak}$ between peak of orbital frequency and peak of radiation mimics what one observes in the test-particle limit using BH perturbation theory [56–58]. The input values are fits to NR that depend on ν and the variable χ [7,45],

$$\chi\equiv\frac{\chi_{\rm Kerr}}{1-2\nu}=\chi_{\rm S}+\frac{\chi_{\rm A}}{1-2\nu}\delta. \tag{2.8}$$

Explicit formulas for the input values can be found in Appendix A.

The EOB GW radiation-reaction force $\mathcal{F}$ is modeled adding up the amplitudes of the factorized modes themselves [13,15,19,51]

$$\mathcal{F}\equiv\frac{\Omega}{16\pi}\frac{\boldsymbol{p}}{|\boldsymbol{L}|}\sum_{\ell=2}^{8}\sum_{m=-\ell}^{\ell}m^2|D_{\rm L}h_{\ell m}^{\rm insp\text{-}plunge}|^2, \tag{2.9}$$

where $D_{\rm L}$ is the luminosity distance of the BBH to the observer. Whereas in previous versions of the EOBNR model the NQC factor N_{22} was included in the computation of the radiation-reaction force $\mathcal{F}$, here we only apply it to the (2,2) waveform after the orbital dynamics has been computed without this factor. This has the advantage of speeding up the generation of waveforms, since it avoids the costly procedure of determining the NQC coefficients in an iterative manner, as outlined in Ref. [45], while still providing the correct merger signal.

Reference [13] provided an algorithm to set up inspiraling quasicircular initial conditions for a generic BBH within the EOB approach. One can then numerically evolve such initial conditions by solving Hamilton's equations for $H_{\rm EOB}$, supplemented by the nonconservative force in Eq. (2.9). The evolution is carried out until the light-ring (or photon-orbit) crossing.

C. Merger-ringdown waveforms

The description of the ringdown (RD) signal differs significantly from that of Refs. [7,45]. Here, instead of employing a linear combination of quasinormal modes (QNMs) of the remnant BH that forms after merger, we use a simple analytic ansatz in the spirit of Refs. [59–61]. We use the full catalog of NR waveforms presented in Sec. III (including the Teukolsky waveforms described in Sec. III C) to determine the free coefficients in the model. A detailed study of the accuracy of the phenomenological model that we present below as well as comparison with the model of Ref. [61] is presented in Appendix B. Here, we simply summarize the main conclusions, namely that our model allows us to faithfully reproduce the ringdown signal of NR waveforms across the NR catalog: replacing the NR ringdown by our model and computing the mismatch against the original NR waveform at a total mass such that the peak of the waveform is at 50 Hz (so that the ringdown falls in the most sensitive frequency band of the detector), we obtain values below 0.001 across the NR catalog with typical values around 10^{-4} (see Fig. 12 below). By comparison, the distribution obtained with the model presented in Ref. [61] (which was only calibrated to a subset of the NR catalog used here) peaks close to 0.001 and features a tail extending above 1%.

The RD waveform is attached to the inspiral-plunge waveform at its amplitude peak, that is at time $t^{22}_{\rm match}\equiv t^{22}_{\rm peak}$, where the NQC correction guarantees agreement with the NR input values. For $t\geq t^{22}_{\rm match}$, we define

$$h_{22}^{\rm merger\text{-}RD}(t)=\nu\tilde{A}_{22}(t)e^{i\tilde{\phi}_{22}(t)}e^{-i\sigma_{220}(t-t^{22}_{\rm match})}, \tag{2.10}$$

where σ_{220} is the least-damped QNM of the BH that forms after merger. We denote $\sigma^R\equiv{\rm Im}\sigma_{220}<0$ and $\sigma^I\equiv-{\rm Re}\sigma_{220}<0$. The value of σ_{220} is computed from Ref. [62] using the final mass and spin of the remnant.

These, in turn, are computed using fitting formulas that connect the masses and spins of the initial BBH to the properties of the final object. In particular, we employ the same final mass formula of Ref. [7], which is based on Refs. [63,64]. We use the final spin formula of Ref. [65], which collected 619 NR simulations available in the literature.

The amplitude term $\tilde{A}_{22}$ and the phase term $\tilde{\phi}_{22}$ are simple analytic ansätze described below with free coefficients fitted to our catalog of NR simulations.

Finally, the complete inspiral-merger-ringdown signal is given by

$$h_{22}(t) = h_{22}^{\text{insp-plunge}}(t)\theta(t_{\text{match}}^{22} - t) + h_{22}^{\text{merger-RD}}(t)\theta(t - t_{\text{match}}^{22}). \quad (2.11)$$

1. Merger-ringdown amplitude

To model the RD amplitude, we use the same ansatz of Ref. [60]

$$\tilde{A}_{22}(t) \equiv c_1^c \tanh\left[c_1^f (t - t_{\text{match}}^{22}) + c_2^f\right] + c_2^c. \quad (2.12)$$

The superscripts c stand for "constrained" as these coefficients are fixed by imposing that the amplitude is of class C^1 at the attachment point, while the superscripts f stand for "free" and correspond to coefficients that will be fitted to NR simulations. Requiring that $|h_{22}|$ is of class C^1 at $t = t_{\text{match}}^{22}$ allows us to express c_1^c and c_2^c as functions of c_1^f, c_2^f, σ^R, $|h_{22}^{\text{insp-plunge}}(t_{\text{match}}^{22})|$, and $\partial_t |h_{22}^{\text{insp-plunge}}|(t_{\text{match}}^{22})$. Note that the last two values match the NR input values thanks to the NQC corrections to the merger waveform. In particular, $\partial_t |h_{22}^{\text{insp-plunge}}|(t_{\text{match}}^{22}) = 0$ since the attachment is done at the amplitude peak of the inspiral-plunge waveform.

After plugging these constraints in Eq. (2.12), we are left with a function of the two free parameters $c_{1,2}^f$, which can be determined for each point in parameter space (ν, χ_1, χ_2) where we have a NR waveform by performing a least-squares fit. The resulting values are well represented using simple polynomial fits

$$c_1^f = -0.0893454\nu^2 + 0.0612892\nu + 0.00146142\nu\chi - 0.0136459\chi^2 - 0.0196758\chi + 0.0830664, \quad (2.13)$$

$$c_2^f = -1.82173\nu^2 - 5.25339\nu^2\chi + 2.40203\nu\chi + 1.39777\nu - 0.371365\chi - 0.623953. \quad (2.14)$$

Note that the amplitude is only smooth up to its first derivative at the attachment point.

2. Merger-ringdown phase

To model the RD phase, we find that a slightly simplified version of the ansatz proposed in Ref. [60], namely

$$\tilde{\phi}_{22}(t) = \phi_0 - d_1^c \log\left[\frac{1 + d_2^f e^{-d_1^f (t - t_{\text{match}}^{22})}}{1 + d_2^f}\right], \quad (2.15)$$

is sufficient to accurately reproduce the NR waveforms. We impose that the phase is C^1 at the attachment point (i.e., the GW frequency is C^0). This allows us to express d_1^c in terms of d_1^f, d_2^f, σ^I, and the GW frequency at the attachment point $\omega_{22}^{\text{insp-plunge}}(t_{\text{match}}^{22})$. Here, ϕ_0 trivially corresponds to the phase of the inspiral-plunge waveform at t_{match}^{22}. Note that $\omega_{22}^{\text{insp-plunge}}(t_{\text{match}}^{22})$ is set equal to the corresponding NR input value by the NQC corrections. Values for $d_{1,2}^f$ are then obtained for each NR waveform in the catalog using a least-squares fit. The resulting values are again well represented by simple polynomials

$$d_1^f = -0.808987\nu^2 + 0.263456\nu - 0.120853\nu\chi - 0.0244358\chi^2 + 0.00779176\chi + 0.147584, \quad (2.16)$$

$$d_2^f = +17.5646\nu^2 - 6.99396\nu - 9.61861\nu\chi + 0.581626\chi^2 + 3.13067\chi + 2.46654. \quad (2.17)$$

Note that these expressions guarantee a monotonic evolution of the frequency after the attachment point.

In Appendix B we discuss the accuracy of this phenomenological RD model and compare it with the RD model of Ref. [61].

III. NUMERICAL-RELATIVITY AND BLACK-HOLE-PERTURBATION-THEORY WAVEFORMS

To calibrate the inspiral-plunge part of EOB waveforms we use 140 NR waveforms [39] generated by the (pseudo) Spectral Einstein code (SpEC) of the Simulating eXtreme Spacetime (SXS) project, and 1 NR waveform [42] produced by the BAM code. We also incorporate information from merger waveforms computed in BH perturbation theory [56,57]. After calibration, we further assess the accuracy of the EOBNR waveforms by comparing them to 4 waveforms produced by the SpEC code and 2 by the Einstein Toolkit code. Those waveforms were generated for this paper.

In Fig. 1 we show, in the intrinsic BBH parameter space, the location of the NR and BH-perturbation-theory waveforms employed to build the new EOBNR model (SEOBNRv4) and the previous EOBNR model (SEOBNRv2), as well.

A. Numerical-relativity methods

SpEC [67–70] is a pseudospectral code capable of efficiently solving many types of elliptic and hyperbolic differential equations, with the primary goal of modeling compact-object binaries. For smooth problems, spectral

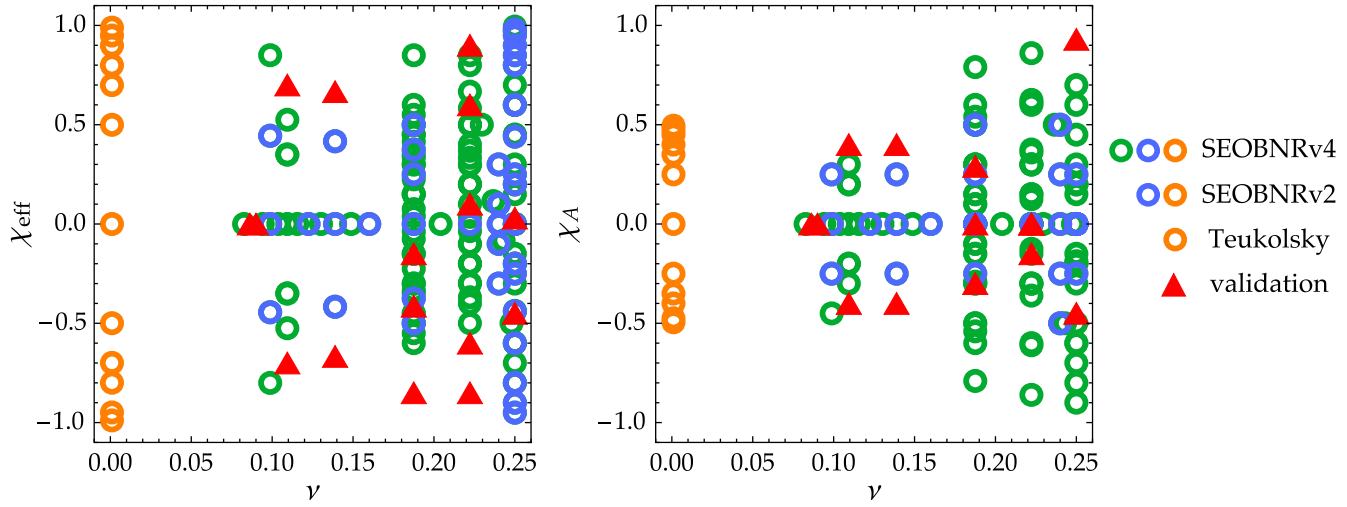

FIG. 1. Numerical-relativity [38–42,66] and Teukolsky [57] waveforms used for calibration and validation of the EOBNR waveform model. We project the 3D parameter space of spinning, nonprecessing waveforms using the symmetric mass ratio ν and two BH spin combinations: $\chi_{\rm eff} \equiv (m_1\chi_1 + m_2\chi_2)/M$ and $\chi_{\rm A} \equiv (\chi_1 - \chi_2)/2$. We note the better coverage of the large, positive $\chi_{\rm eff}$ region and of the $\chi_{\rm A}$ dimension in the NR catalog used to calibrate the EOBNR model of this paper (SEOBNRv4) with respect to the one used in the EOBNR model of Ref. [7] (SEOBNRv2). Red triangles indicate NR waveforms used for validation of the calibration.

methods are exponentially convergent and high accuracy can be achieved even for long simulations. SpEC evolves the first order formulation [71] of the generalized harmonic formulation of Einstein's equations [72,73]. The damped harmonic gauge [74] is used to provide stable coordinate conditions. Singularities inside BHs are dynamically excised from the computational domain using feedback control systems [41,75]. SpEC uses h-p adaptivity to dynamically control numerical truncation error and to increase computational efficiency [76]. Waveforms are extracted using the Regge-Wheeler-Zerilli formalism on a series of coordinate spherical shells and extrapolated to null infinity using polynomial expansions in powers of the areal radius [77].

The Einstein Toolkit [78] is a collection of open source NR components built around the Cactus framework [79]. The initial data is computed in the Bowen-York formalism [80,81] using TwoPunctures [82], with low eccentricity parameters determined through our implementation of [83] for the Einstein Toolkit. The time evolution is performed in the BSSN [84–86] formulation of the Einstein equations using McLachlan [87], and the BHs are evolved with the coordinate conditions of the moving-puncture method [88,89] using 8th order accurate finite differencing. Adaptive mesh refinement, in which regions of high resolution follow the BHs, is provided by Carpet [90]. The near zone is computed using Cartesian grids, and the wave zone is computed on spherical grids using the Llama multipatch infrastructure [91], enabling the efficient computation of high-accuracy waveforms at large distances from the source. Apparent horizons are computed using AHFinderDirect [92] and spins are computed in the dynamical horizon formalism using QuasiLocalMeasures [93]. Gravitational waves are computed using WeylScal4, and the GW strain h is computed from the Newman-Penrose curvature component Ψ_4 at finite radius $r \in [100M, 500M]$ using fixed-frequency integration [94] with a cutoff frequency equal to $3/4$ the initial waveform frequency, and extrapolated to $\mathcal{J}^+$ using second and first order extrapolation for the amplitude and phase, respectively. WeylScal4 and McLachlan are both generated using the Kranc [95] automated-code-generation package. Simulations are managed using the Simulation Factory [96], and the BBH evolution parameters are based on the open source Einstein Toolkit GW150914 example [97]. Analysis and postprocessing is performed using the open-source SimulationTools [98] for *Mathematica*.

The bam code [99,100] uses broadly the same methods as the Einstein Toolkit but, with the exception of the TwoPunctures initial data solver, was developed independently. The spatial derivatives are discretized using 6th order accurate finite differencing, and the wave zone is computed on Cartesian grids.

B. Numerical-relativity waveforms

We use a total of 157 NR waveforms: 141 for calibrating the model and 16 for validation. The full list can be found in Appendix C, which contains separate tables for the different data sets that constitute our catalog. Here, we give a brief description of each set, denoting with $\{C, V\} = \{141, 16\}$ the number of simulations used for calibration and validation in each of them.

A first set of $\{38, 0\}$ waveforms belongs to the original SXS public catalog [38,67], which was also used to

TABLE I. We display the binary configurations of the new NR simulations produced for this paper. Those used for calibration of the new model are shown first, followed by those used for validation, separated by a horizontal line. Shown are the mass ratio $q = m_1/m_2$, the dimensionless spins $\chi_{1,2} = (\boldsymbol{S}_{1,2} \cdot \hat{\boldsymbol{L}}_N)/m_{1,2}^2$, the eccentricity e, the initial frequency of the $(\ell, m) = (2, 2)$ mode of the waveform strain ω_{22}, and the number of orbits (up to the waveform peak) $N_{\rm orb}$. All quantities are measured at an early time after the effects of junk radiation are no longer important.

ID	q	χ_1	χ_2	e	$M\omega_{22}$	$N_{\rm orb}$
SXS:BBH:0610	1.2	−0.50	−0.50	7.4×10^{-5}	0.01872	12.1
SXS:BBH:0611	1.4	−0.50	+0.50	6.0×10^{-4}	0.02033	12.5
SXS:BBH:0612	1.6	+0.50	−0.50	3.7×10^{-4}	0.02156	12.8
SXS:BBH:0613	1.8	+0.50	+0.50	1.8×10^{-4}	0.02383	13.1
SXS:BBH:0614	2.0	+0.75	−0.50	6.7×10^{-4}	0.02355	13.1
SXS:BBH:0615	2.0	+0.75	+0.00	7.0×10^{-4}	0.02401	13.3
SXS:BBH:0616	2.0	+0.75	+0.50	8.0×10^{-4}	0.02475	13.3
SXS:BBH:0617	2.0	+0.50	+0.75	7.8×10^{-4}	0.02342	13.1
SXS:BBH:0618	2.0	+0.80	+0.80	5.9×10^{-4}	0.02578	13.4
SXS:BBH:0622	8.0	−0.90	+0.00	1.1×10^{-3}	0.01559	28.0
SXS:BBH:0620	5.0	−0.80	+0.00	3.4×10^{-3}	0.02527	8.2
SXS:BBH:0621	7.0	−0.80	+0.00	3.2×10^{-3}	0.02784	7.1
SXS:BBH:0619	2.0	+0.90	+0.90	2.9×10^{-4}	0.02520	13.5
ET:AEI:0001	5.0	+0.80	+0.00	9.2×10^{-4}	0.03077	10.5
ET:AEI:0002	7.0	+0.80	+0.00	6.1×10^{-4}	0.03503	10.4
ET:AEI:0004	8.0	+0.85	+0.85	3.0×10^{-3}	0.04368	7.4

calibrate the previous EOBNR model [7]. Additional sets of $\{6, 0\}$ long waveforms (between 36 and 88 orbits) with mass ratios 5 and 7 and spins on the largest BH of $\chi_1 = \pm 0.4$ or ± 0.6 (and no spin on the companion) [66] and of $\{2, 1\}$ near equal-mass and near extremal spins [40,41] were subsequently added to our catalog. Another set of $\{84, 10\}$ SXS waveforms were produced in the last few years and are described in Ref. [39]. These waveforms extend the coverage in the region of parameter space with $1 \leq q \leq 3$ to systems where both spin magnitudes go up to 0.85, including many antisymmetric spin configurations. The length of the waveforms ranges between 20 and 40 orbits.

Furthermore, $\{9, 4\}$ new SXS waveforms were produced for this paper and are summarized in Table I. These waveforms can be broadly divided into 2 categories: those filling in the gaps of coverage in the aligned-spin catalogue [39] ($1 < q \leq 2$, $0.5 \leq |\chi_{1,2}| \leq 0.9$), and those extending coverage to even higher mass ratios ($5 \leq q \leq 7$) for single spin binaries where the largest BH has a large antialigned spin ($-0.9 \leq \chi_1 \leq -0.8$). We also use for calibration one waveform with physical parameters $(q, \chi_1, \chi_2) = (8, 0.85, 0.85)$ that was previously produced using BAM [99,100] and it was employed to calibrate the IMRPHENOMD model [34]. However, this waveform was available at only one resolution, was not extrapolated to infinity, and had a relativity high eccentricity of 1.2×10^{-2}. In order to check that these effects were not dominant, we also produced a waveform for this configuration, listed as ET:AEI:0004 in Table I, with the EINSTEIN TOOLKIT including multiple resolutions, extrapolation, and with a lower eccentricity 3.0×10^{-3}. We have found excellent agreement between the waveforms produced with the two codes, and negligible effects due to resolution or extrapolation errors when comparing with the EOBNR waveform. We have also employed the EINSTEIN TOOLKIT to produce two $(q, \chi_1, \chi_2) = (5, 0.8, 0)$ and (7, 0.8, 0) waveforms listed as ET:AEI:0001 and ET:AEI:0002 in Table I. The new waveforms are between 7 and 28 orbits in length and used for validation.

C. Merger-ringdown waveforms from black-hole perturbation theory

Although NR is currently capable of accurately simulating the full coalescence of BBHs at moderately large mass ratios and spins (up to ∼20 and 0.8 [42]), evolutions at even higher mass ratios and larger spin magnitudes are still not tractable within this framework. Nonetheless, for such systems it is possible to extract valuable information from BH perturbation theory. In particular, the merger-RD GW emission of test particles inspiraling and merging into a BH can be modeled by numerical solutions of the Regge-Wheeler-Zerilli [101,102] (Teukolsky [103]) equation, describing metric (curvature) perturbations to Schwarzschild (Kerr) spacetimes. Several studies in recent years [56,57,104] have employed time-domain Teukolsky codes sourced by particles on plunging, equatorial trajectories to compute the dominant and leading subdominant multipolar modes of the merger-RD waveforms.

In this paper, we employ the Teukolsky waveforms of Ref. [57] to build the test-particle-limit fits to the input

values (see Appendix A). This means that we extract amplitude, curvature of the amplitude, GW frequency, and slope of the GW frequency of the (2,2) mode at its peak. Teukolsky waveforms are also used in the construction of the phenomenological RD model described in Sec. II C. Note that we cannot exploit the inspiral portion of Teukolsky waveforms because of the approximations that are involved in the modeling of the perturbing trajectory. In fact, Ref. [57] only used the conservative dynamics of geodesics in Kerr spacetime and the dissipation provided by leading-order BH perturbation theory.

IV. CALIBRATION OF INSPIRAL-PLUNGE PARAMETERS TO NUMERICAL-RELATIVITY WAVEFORMS

Given a point in BBH parameter space $(m_1, m_2, \chi_1, \chi_2)$, the EOB model described in Sec. II provides an inspiral-merger-ringdown (2,2)-mode waveform that depends on four inspiral-plunge calibration parameters. These parameters are: (i) a parameter K that determines the position of the EOB horizon $r_+^{\rm EOB}$ and the shape of the radial potential Δ_u [see Eq. (2.2)] in the strong-field region below and around the ISCO, (ii) a 4.5PN spin-orbit parameter $d_{\rm SO}$ that enters the EOB spin mapping between the real and effective descriptions, (iii) a 3PN spin-spin parameter $d_{\rm SS}$ that enters the EOB spin mapping, and (iv) a parameter $\Delta t^{22}_{\rm peak}$ that determines the time delay between the peak of orbital frequency and the peak of radiation. In this section, we describe how these four parameters are tuned to NR waveforms.

A. Calibration requirements

The goal of the calibration is to obtain EOB waveforms that can be employed in the analysis of current ground-based interferometric data with negligible impact from mismodeling errors, at least in the region of parameter space where BBH configurations have been simulated in full NR. Two are the main applications of waveform approximants, namely template-based detection pipelines and parameter estimation of GW sources—including parametrized tests of general relativity. Template banks [3,5,6] that are employed by LIGO-Virgo in matched-filtering searches of binary coalescences are built requiring that the loss in signal-to-noise ratio due to the discrete nature of the bank is smaller than 3% [5], which translates into a loss in detections smaller than 10%. On the other hand, in the context of parameter estimation, the correct assessment of biases due to waveform modeling inaccuracies requires a full-fledged Bayesian inference. In fact, no simple waveform accuracy requirements can be formulated and the criterion of indistinguishability proposed in Ref. [105] is a sufficient, but not necessary criterion, and it has been shown to be highly restrictive [106,107]. Here, we do not aim at addressing the question of whether our EOBNR waveform model is completely free of biases. As done in previous studies [7,22,23,26], we adopt the simplified criterion of requiring that the EOBNR waveforms have matches with NR waveforms—in the sense specified below—above 99% when the optimization is done only on a global phase and time shift.

Given two waveforms $h_1(t)$ and $h_2(t)$, their noise-weighted overlap or match is defined as [108]

$$(h_1|h_2) \equiv 4\mathrm{Re}\int_{f_l}^{f_h} \frac{\tilde{h}_1(f)\tilde{h}_2^*(f)}{S_n(f)}\mathrm{d}f, \tag{4.1}$$

with $\tilde{h}_{1,2}(f)$ indicating the Fourier transforms of the waveforms and $S_n(f)$ the one-sided power spectral density (PSD) of the detector noise. The *faithfulness* is then defined as the overlap between the normalized waveforms maximized over relative time and phase shifts

$$\langle h_1|h_2\rangle = \max_{\phi_c,t_c} \frac{(h_1(\phi_c,t_c)|h_2)}{\sqrt{(h_1|h_1)(h_2|h_2)}}. \tag{4.2}$$

Another useful notion is that of *effectualness*, defined as the maximum faithfulness of a waveform against a template bank. This amounts to maximizing the faithfulness over a discrete set of intrinsic physical parameters. For the calibration of the model to NR, we use the design zero-detuned high-power noise PSD of Advanced LIGO [109]. We choose f_l as the starting GW frequency after the junk radiation has settled in the NR simulation,[1] and $f_h = 3$ kHz. We taper the waveforms in the time domain (before transforming to the frequency domain) using a hyperbolic-tangent window function to reduce spectral leakage [110]. Let

$$\boldsymbol{\theta} \equiv \{K, d_{\rm SO}, d_{\rm SS}, \Delta t^{22}_{\rm peak}\} \tag{4.3}$$

denote the set of inspiral-plunge calibration parameters, and

$$\boldsymbol{\lambda} \equiv \{m_1, m_2, \chi_1, \chi_2\} \tag{4.4}$$

the set of intrinsic BBH parameters. In practice, the intrinsic parameter space is only 3-dimensional (q, χ_1, χ_2), because BBH waveforms scale trivially with the total mass M. Since we work with dominant-mode nonprecessing waveforms, we perform all calculations omitting extrinsic BBH parameters (such as inclination, sky location, polarization, etc.). We denote the faithfulness of $h_{\rm EOB}$ to $h_{\rm NR}$, at given values of the calibration parameters $\boldsymbol{\theta}$, as

$$\mathcal{M}(\boldsymbol{\theta}) = \langle h_{\rm EOB}(\boldsymbol{\lambda};\boldsymbol{\theta})|h_{\rm NR}(\boldsymbol{\lambda})\rangle. \tag{4.5}$$

Note that the comparison is done between waveforms with the same intrinsic parameters $\boldsymbol{\lambda}$. The *unfaithfulness* is defined as $\bar{\mathcal{M}}(\boldsymbol{\theta}) \equiv 1 - \mathcal{M}(\boldsymbol{\theta})$.

[1] If the starting frequency is lower than 10 Hz, we use $f_l = 10$ Hz instead.

To guide the waveform calibration, we design a figure of merit which, for each NR waveform in the catalog, is a function of (i) the faithfulness with the corresponding EOBNR waveform, and (ii) the difference $\delta t^{22}_{\rm peak}(\boldsymbol{\theta})$ of the merger time (measured after low-frequency phase alignment between EOB and NR waveforms). We use the time when the amplitude peaks as a proxy for the merger time. For each configuration in the NR catalog, our goal is to find values of $\boldsymbol{\theta}$ such that $\mathcal{M} \geq 99\%$ and $|\delta t^{22}_{\rm peak}| \leq 5M$. Note that the requirement on $\delta t^{22}_{\rm peak}$ aims at taming time-domain dephasings at merger, something to which $\mathcal{M}$ is not very sensitive.

B. Markov-chain Monte Carlo analysis

Given the dimensionality of our calibration parameter space, a naive approach aiming at covering it with a regular grid is highly inefficient and not feasible in practice. One alternative, used in previous calibrations of the model [7,22], is to resort to local optimization algorithms (such as the numerical simplex method) which can efficiently converge to minima of our figure of merit (and to minima with values of the figure of merit satisfying our calibration requirements provided that good initial conditions are chosen). This however only provides us with best-fit values for each numerical configuration but with no notion of how much we can deviate from those values without degrading the figure of merit below some threshold. In the present work, we aim at using more information on the structure of our calibration space, and in particular on the correlations between our calibration parameters.

In general, Markov-chain Monte Carlo (MCMC) methods are well suited to exploring high-dimensional parameter spaces with limited computational costs [111]. Here, we employ the EMCEE[2] [112] package, which is a PYTHON implementation of an affine-invariant MCMC ensemble sampler [113]. This algorithm has better performance over traditional MCMC sampling methods (e.g., the traditional Metropolis-Hasting method), as measured by the smaller autocorrelation time and fewer hand-tuning input parameters. It transforms the sampling of the parameter space by an affine transformation such that the internal algorithm samples an isotropic density, so it is insensitive to covariances among parameters. This is achieved by the "stretch move," that simultaneously evolves an ensemble of walkers, and determines a walker's next proposal distribution (i.e., the next possible move) by current positions of the other walkers in the complementary ensemble (for more details, see Refs. [112,113]).

For each NR simulation, we want to obtain a posterior distribution in $\boldsymbol{\theta}$-space whose mean and variance (and mutual correlations between the θ^j's) relate to the calibration requirements described in Sec. IV A. In the MCMC sampler, we need to assign the probability to accept a possible move of the kth walker from an old position $\boldsymbol{\theta}^{(\rm old)}_k$ to a new position, $\boldsymbol{\theta}^{(\rm new)}_k = \boldsymbol{\theta}_j + Z[\boldsymbol{\theta}^{(\rm old)}_k - \boldsymbol{\theta}_j]$, with the jth walker randomly drawn from the remaining walkers, and Z a random variable drawn from a distribution $g(z)$ (whose expression is given in Eq. (10) of Ref. [112]). To satisfy the detailed balance condition, the probability for the move is $\min[1, Z^{N-1} P(\boldsymbol{\theta}^{(\rm new)}_k)/P(\boldsymbol{\theta}^{(\rm old)}_k)]$, with N the dimension of the parameter space ($N = 4$ for our $\boldsymbol{\theta}$-space), and $P(\boldsymbol{\theta})$ the likelihood function. For each NR run, we choose the likelihood function to be,

$$P(\boldsymbol{\theta}) \propto \exp\left[-\frac{1}{2}\left(\frac{\bar{\mathcal{M}}_{\rm max}(\boldsymbol{\theta})}{\sigma_{\mathcal{M}}}\right)^2 - \frac{1}{2}\left(\frac{\delta t^{22}_{\rm peak}(\boldsymbol{\theta})}{\sigma_t}\right)^2\right], \quad (4.6)$$

where $\bar{\mathcal{M}}_{\rm max}(\boldsymbol{\theta})$ is, for a given $\boldsymbol{\theta}$, the maximum unfaithfulness of EOB to NR over the total mass range $10\,M_\odot \leq M \leq 200\,M_\odot$, $\sigma_{\mathcal{M}}$ is chosen to be 1%, and σ_t is chosen to be $5M$, consistently with our calibration requirements.

We carry out the calibration employing the 140 SXS NR waveforms plus 1 BAM NR waveform, as presented in Sec. III. Furthermore, after calibration we use 6 NR waveforms with parameters $(q, \chi_1, \chi_2) = (1.3, 0.96, -0.9)$, $(2, 0.9, 0.9)$, $(5, -0.8, 0)$, $(5, 0.8, 0)$, $(7, -0.8, 0)$, $(7, 0.8, 0)$ to test and validate the EOBNR waveform model. Initial values of $\boldsymbol{\theta}$ were constructed with the help of a coarse grid for each NR waveform. For each NR simulation, we used 44 walkers and accumulated $\sim 40,000$ points, a number large enough to result in well sampled posteriors while keeping the computational cost manageable.

For each chain in $\boldsymbol{\theta}$-space, we discard the first half of the points, as the burn-in phase of the MCMC run [114]. We also discard points with $\bar{\mathcal{M}}_{\rm max} > 1\%$ and $|\delta t^{22}_{\rm peak}| > 5M$. The 2D projections of these 4D distributions were then examined by eye. Some cases featured a secondary mode, notably in the parameter K. To simplify the analysis presented in Sec. IV C where a multidimensional Gaussian distribution is assumed, some modes are pruned away by hand. For example, we consistently keep the points in the chains that correspond to smaller K if a secondary (higher) mode exists. From the remaining points, we extract the vector of the means $\langle\boldsymbol{\theta}\rangle_{(n)}$ and the covariance matrices $\mathcal{C}_{(n)}$, where n labels the NR simulation. To check that simply taking the mean of each 1D posterior provides a good calibration point for each configuration, we compute the faithfulness between the EOBNR and NR waveforms using $\boldsymbol{\theta} = \langle\boldsymbol{\theta}\rangle_{(n)}$ and find a worst value over the catalog $\gtrsim 99.5\%$. Thus, in the next section we fit the means $\langle\boldsymbol{\theta}\rangle_{(n)}$—using error bars constructed from the covariances $\mathcal{C}_{(n)}$—to obtain expressions for our calibration parameters as functions of the physical parameters.

[2] http://dan.iel.fm/emcee.

C. Interpolation and extrapolation to the entire BBH parameter space

We now discuss how we interpolate between and extrapolate away from the 141 BBH configurations spanned by the NR catalog. We want K, $d_{\rm SO}$, $d_{\rm SS}$, and $\Delta t^{22}_{\rm peak}$ to be prescribed functions of (q,χ_1,χ_2) that best fit the means $\langle\boldsymbol{\theta}\rangle_{(n)}$. For simplicity, we only consider polynomial fitting functions that depend on ν and the spin combination χ [defined in Eq. (2.8)], similarly to what was done for fits of the input values and of the ringdown waveforms.

First, we want to fix the nonspinning limit of the calibration parameters. However, this is only possible for K and $\Delta t^{22}_{\rm peak}$, since for nonspinning BBH configurations the EOB waveforms do not depend on $d_{\rm SO}$ and $d_{\rm SS}$. Let $\mathcal{S}_{\rm ns}$ be the set of 17 nonspinning NR runs that are present in the catalog. Let $\boldsymbol{\theta}_{\rm ns}\equiv\{K,\Delta t^{22}_{\rm peak}\}$ and $\mathcal{C}_{\rm ns}$ be the 2×2 covariance matrix restricted to the $\boldsymbol{\theta}_{\rm ns}$-space. We parametrize K and $\Delta t^{22}_{\rm peak}$ with polynomials that are at most cubic in ν. We determine the coefficients of these polynomials by minimizing the following quantity:

$$\chi^2_{\rm ns}\equiv\sum_{n\in\mathcal{S}_{\rm ns}}\frac{1}{2}(\boldsymbol{\theta}_{\rm ns}-\langle\boldsymbol{\theta}_{\rm ns}\rangle_{(n)})(\mathcal{C}^{-1}_{\rm ns})_{(n)}(\boldsymbol{\theta}_{\rm ns}-\langle\boldsymbol{\theta}_{\rm ns}\rangle_{(n)})^{\rm T}+\chi^2_{\rm TPL}, \tag{4.7}$$

where the last term enforces that K and $\Delta t^{22}_{\rm peak}$ approach their test-particle limits [7,57], 1.712 and $-2.5M$, respectively. We obtain that the nonspinning fits of K and $\Delta t^{22}_{\rm peak}$ read

$$\begin{aligned}K|_{\chi=0}=&+267.788247\nu^3-126.686734\nu^2\\&+10.257281\nu+1.733598,\end{aligned} \tag{4.8}$$

and

$$\begin{aligned}\left.\frac{\Delta t^{22}_{\rm peak}}{M}\right|_{\chi=0}=&+716.044155\nu^3-13.087878\nu^2\\&-45.883834\nu-2.504992.\end{aligned} \tag{4.9}$$

Let us now consider the problem of fitting the means of the calibration parameters over $\mathcal{S}_{\rm spin}$, the set of spinning NR simulations. We now work in $\boldsymbol{\theta}$-space, and parametrize each θ^j with a polynomial that is at most cubic in ν and χ, making sure that the nonspinning limits in Eqs. (4.8) and (4.9) are satisfied. To determine the coefficients of the fitting polynomials, we devise a quantity to be minimized, $\chi^2_{\rm spin}$, containing three terms: (i) a term that restricts the domain of the four calibration parameters, (ii) a term that penalizes deviations from the test-particle limit of $\Delta t^{22}_{\rm peak}$ (see the (2,2)-mode curve in Fig. 13 of Ref. [57]), and (iii) a term that depends on the MCMC means and covariances, of the form

$$\sum_{n\in\mathcal{S}_s}\frac{w}{2}(\boldsymbol{\theta}-\langle\boldsymbol{\theta}\rangle_{(n)})\mathcal{C}^{-1}_{(n)}(\boldsymbol{\theta}-\langle\boldsymbol{\theta}\rangle_{(n)})^{\rm T}, \tag{4.10}$$

where w is a weighting function that reads

$$w\equiv\chi_1^2+\chi_2^2+\frac{|\chi|}{2\nu}. \tag{4.11}$$

The introduction of the weighting function w is necessary to empirically account for the inhomogeneous distribution of NR simulations in the BBH parameter space, their different length and to improve the faithfulness of the model against NR waveforms with large aligned-spin components. The minimization of $\chi^2_{\rm spin}$ was performed with the Nelder-Mead downhill simplex algorithm [115], giving

$$\begin{aligned}K=&-59.165806\chi^3\nu^3-0.426958\chi^3\nu+1.436589\chi^3\\&+31.17459\chi^2\nu^3+6.164663\chi^2\nu^2-1.380863\chi^2\\&-27.520106\chi\nu^3+17.373601\chi\nu^2+2.268313\chi\nu\\&-1.62045\chi+K|_{\chi=0},\end{aligned} \tag{4.12}$$

$$\begin{aligned}d_{\rm SO}=&+147.481449\chi^3\nu^2-568.651115\chi^3\nu\\&+66.198703\chi^3-343.313058\chi^2\nu\\&+2495.293427\chi\nu^2-44.532373,\end{aligned} \tag{4.13}$$

$$\begin{aligned}d_{\rm SS}=&+528.511252\chi^3\nu^2-41.000256\chi^3\nu\\&+1161.780126\chi^2\nu^3-326.324859\chi^2\nu^2\\&+37.196389\chi\nu+706.958312\nu^3\\&-36.027203\nu+6.068071,\end{aligned} \tag{4.14}$$

$$\begin{aligned}\frac{\Delta t^{22}_{\rm peak}}{M}=&-0.192775\chi^3\nu^2+19.053803\chi^3\nu\\&-11.543497\chi^2+40.318332\chi\nu\\&-13.006363\chi+\left.\frac{\Delta t^{22}_{\rm peak}}{M}\right|_{\chi=0}.\end{aligned} \tag{4.15}$$

In the above expressions, we notice that not all powers of ν and χ up to cubic order are present. Indeed, we were able to set to zero some of the terms without degrading the performance of the fit, demonstrating that not all powers are necessary to represent the data. For example, the expression of $d_{\rm SO}$ in Eq. (4.13) only contains six terms instead of the sixteen allowed when simply restricting to cubic order polynomials in ν and χ.

D. Performance against the numerical-relativity catalog

Having completed the calibration procedure, we now investigate the performance of our final EOBNR model by computing its faithfulness against the NR catalog, including the 16 test cases that were not used in the calibration. Note that

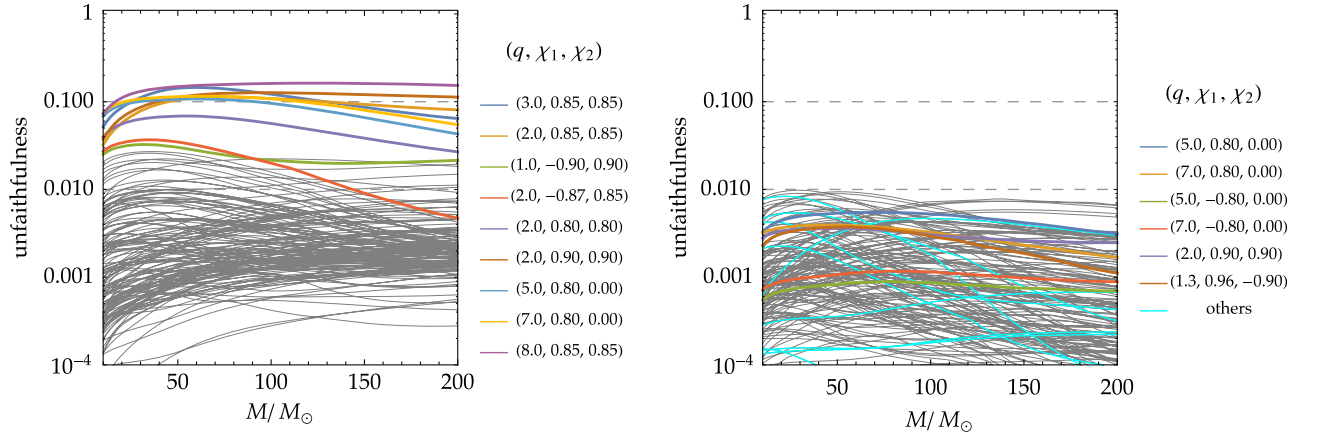

FIG. 2. Unfaithfulness of the EOBNR model of Ref. [7] (SEOBNRv2) (*left panel*) and the EOBNR model of this paper (SEOBNRv4) (*right panel*) against the NR catalog for total masses $10\,M_\odot \leq M \leq 200\,M_\odot$, using the Advanced LIGO design zero-detuned high-power noise PSD and a low-frequency cutoff equal to the initial geometric frequency of each NR run. In the left panel, the cases where the maximum unfaithfulness is >3% are highlighted in color and labeled by (q, χ_1, χ_2). In the right panel, the cases that were not used in the calibration are highlighted with colors and 6 cases whose parameters lie close to the boundary of our calibration domain are singled out in the legend. We note that the new EOBNR model (SEOBNRv4) has unfaithfulness below 1% against the *whole* NR catalog.

6 of these cases lie close to the boundary of the calibration domain. Matches are computed using the setup described above Eq. (4.2). In particular, the design zero-detuned high-power noise PSD of Advanced LIGO [109] is used with a lower frequency cutoff corresponding to the initial geometric frequency of each NR waveform.

In order to put results into context, in the left panel of Fig. 2 we first show the comparison between NR and the previous instance of the spinning, nonprecessing EOBNR model [7] (SEOBNRv2), which was calibrated in 2013 to 38 NR waveforms (see Fig. 1). As was already pointed out in Ref. [35], this model performs very well against most of the NR simulations that became available after its calibration, but the faithfulness degrades noticeably for binaries with unequal masses (∼2–3) and large positive aligned-spin components (∼0.8), with some cases reaching an unfaithfulness of more than 10%. By contrast, our calibrated EOBNR model (SEOBNRv4) (displayed in the right panel of Fig. 2) agrees to better than 1% with all NR simulations. These results are summarized in Fig. 3, where, for both models, the distribution of the maximum unfaithfulness across the mass range $10\,M_\odot \leq M \leq 200\,M_\odot$ for each NR runs is represented as a histogram.

While the faithfulness is the quantity of interest for parameter-estimation applications, it can sometimes hide inaccuracies in the waveform (that can be reabsorbed by time and phase shifts). As a further illustration of the excellent agreement between our new EOBNR model and NR, in Fig. 4 we overlay both waveforms for the $(q, \chi_1, \chi_2) = (3, 0.85, 0.85)$ configuration after phase aligning at low frequency. We see that the new EOBNR model accurately reproduces the full phase evolution through merger and ringdown, and that quantities such as the time to merger are also well predicted. This is due to the inclusion of the second term in Eq. (4.6).

V. COMPARISON WITH WAVEFORM MODELS USED IN THE FIRST OBSERVING RUN OF ADVANCED LIGO

In this section, we compare our EOBNR model (SEOBNRv4) across parameter space (i.e., not restricting to masses and spins for which NR waveforms are available) with the spinning, nonprecessing models that were used for

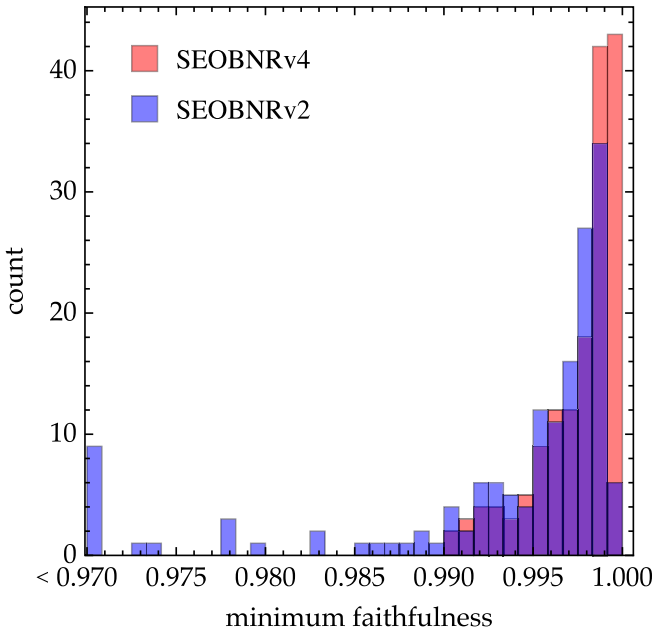

FIG. 3. Distribution of minimum faithfulness of the old EOBNR model (SEOBNRv2) [7] and new EOBNR model (SEOBNRv2) against the NR catalog. The total mass range considered is $10\,M_\odot \leq M \leq 200\,M_\odot$. The calculations are done with the Advanced LIGO design zero-detuned high-power noise PSD and a low-frequency cutoff corresponding to the initial geometric frequency of each NR simulation.

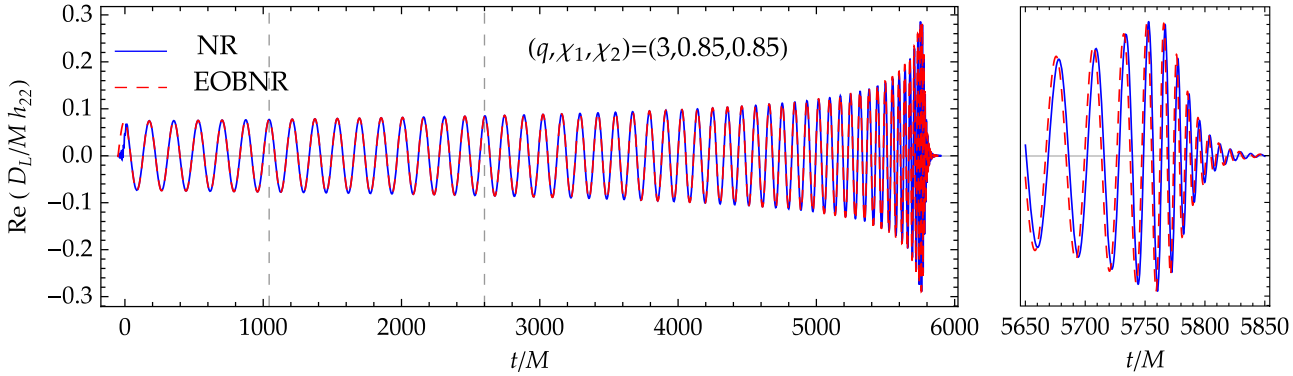

FIG. 4. Waveform comparison in the time domain between the (dominant mode) EOBNR waveform of this paper (SEOBNRv4) (dashed red) and the NR waveform (solid blue) for a BBH with $(q,\chi_1,\chi_2) = (3, 0.85, 0.85)$. The waveforms are phase aligned and time shifted at low frequency (the alignment window is indicated by the vertical dashed lines). The phase evolution throughout late inspiral, merger, and ringdown is well reproduced, as well as the time to merger.

data analyses during the O1 run [5,28], namely the previous EOBNR model (SEOBNRv2) [7] and the phenomenological inspiral-merger-ringdown model (IMRPHENOMD) [34]. The goal here is very different from that of Sec. IV D, where we aimed at assessing the accuracy of the model to NR simulations. Now, we want to identify regions of parameter space where different models agree—which gives some indication that systematic errors due to mismodeling are small (at least for values of M such that the signals are in band)—or disagree—thus suggesting that there the waveform models need further development.

We carry out two types of comparisons: faithfulness—where models are compared using the same physical parameters—and effectualness—where additional maximization over the physical parameters is performed. While the former informs us on intrinsic differences between the models, the latter is a useful quantity in the context of GW searches, where the incoming data are compared to many templates that (discretely) cover the entire parameter space. Since our goal is to guide data-analysis applications in the forthcoming runs of Advanced LIGO, all overlap computations in this section are performed using the noise PSD of the O1 run with a lower frequency cutoff f_l of 25 Hz [116].

Figure 5 summarizes the results of the faithfulness comparison of SEOBNRv4 against SEOBNRv2 and IMRPHENOMD. In each case, 2×10^5 configurations are randomly drawn with component masses uniformly distributed in $1\ M_\odot \leq m_{1,2} \leq 200\ M_\odot$ (with the restriction that the total mass is $4\ M_\odot \leq M \leq 200\ M_\odot$) and component spins uniformly distributed in $-1 \leq \chi_{1,2} \leq 1$. The parameter space to explore is 4D (M,ν,χ_1,χ_2). For the purpose of condensing the results into a small number of plots, while still capturing the main features of the comparison, we resort to projections on 2D subspaces and choose two such projections: $(\nu,\chi_{\rm eff} \equiv (m_1\chi_1 + m_2\chi_2)/M)$ and $(\nu,\chi_{\rm A} \equiv (\chi_1 - \chi_2)/2)$ (these are the same y-axes as in Fig. 1). In order to unclutter the plots, we remove all the points with faithfulness >97%. Therefore, the white areas correspond to regions of parameter space where the models agree to better than 3%. The remaining points are colored according to the faithfulness. Note that, whenever points overlap with each other, those with the lowest faithfulness are brought to the front of the plot.

Focusing first on the comparison of SEOBNRv4 with SEOBNRv2 (see the top row of Fig. 5), we see that the model has mostly changed near the equal-mass line for very unequal spins, and for unequal masses in the region where $\chi_{\rm eff}$ is positive and large, which corresponds to positive χ_1, and also to positive $\chi_{\rm A}$. This is the region where the SEOBNRv2 model was extrapolated and where its performance had been known to degrade (see the left panel of Fig. 2), which has now been fixed by calibrating it to NR waveforms in this region. The fraction of points with faithfulness below 97% is only about 8% of the total.

The IMRPHENOMD model was calibrated to a set of BAM and SXS NR waveforms listed Table I in Ref. [34]. The comparison of SEOBNRv4 against IMRPHENOMD (see the bottom row of Fig. 5) shows a wide region where the two models agree. This is not surprising since in those regions of parameter space both models were calibrated to similar NR waveforms. The fraction of points with faithfulness below 97% is only about 7% of the total. The largest disagreement lies in two regions: one with $\chi_{\rm eff} \gtrsim 0.4$ and $\chi_{\rm A} > 0$ and one with $\nu \lesssim 0.03$ and $\chi_{\rm A} \lesssim 0$. For $\nu \gtrsim 0.18$, some mild disagreement—a few percent—arises for unequal-spin systems, where the IMRPHENOMD model is known to lose accuracy (see Fig. 5 of Ref. [35]). The region of parameter space where current spinning, nonprecessing waveform models disagree the most—with faithfulness up to several tens of percents—corresponds to BBHs with very unequal masses and for which the most massive BH has a large positive aligned-spin component. This is expected for at least two reasons. First, the number of cycles to merger from any given frequency increases with the mass ratio and the spin, so systems in this region spend many cycles in band, and are therefore intrinsically more difficult to model. Second, NR

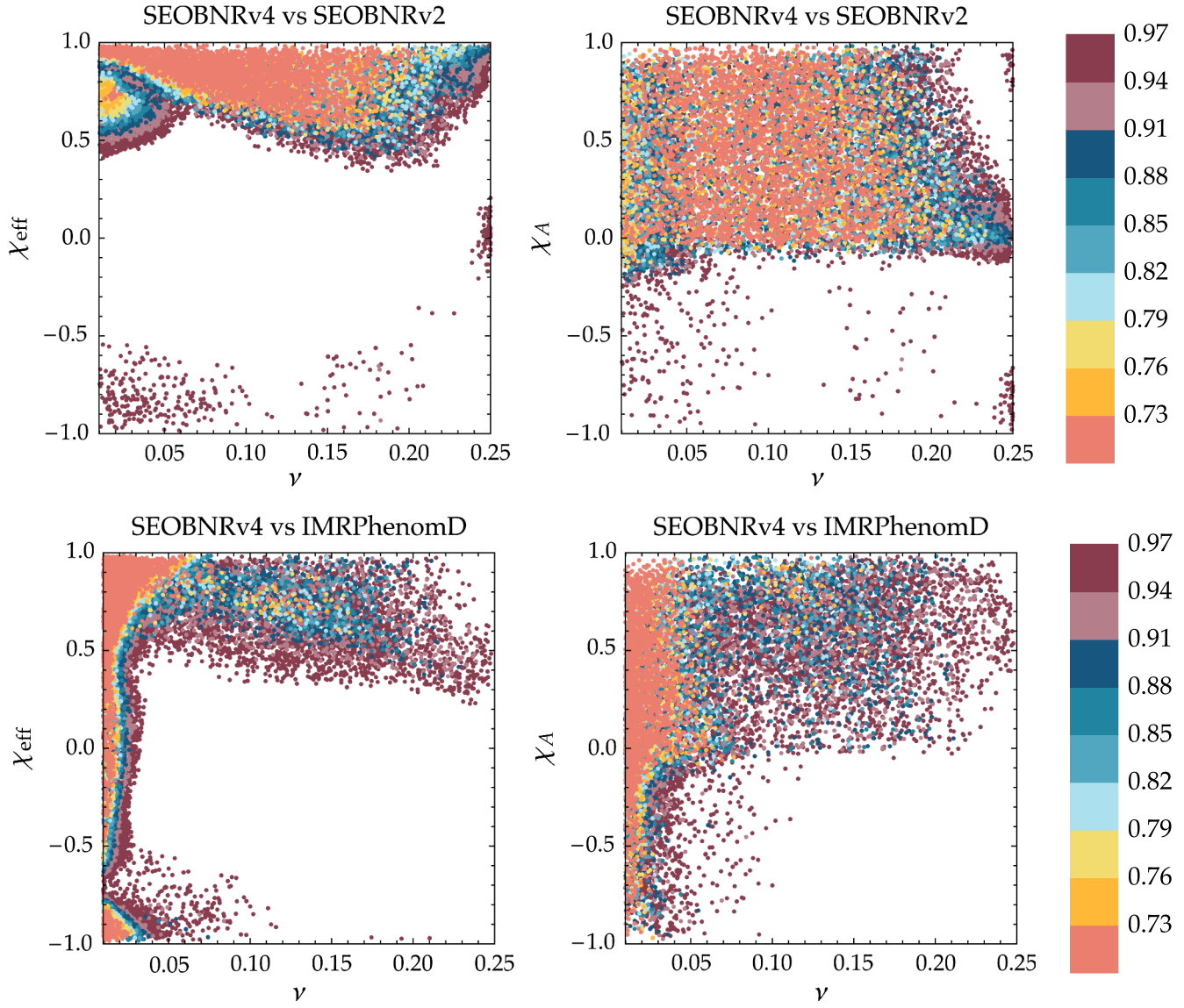

FIG. 5. Faithfulness of the EOBNR model of this paper (SEOBNRv4) against the previous EOBNR model (SEOBNRv2) [7] (*top row*) and the phenomenological inspiral-merger-ringdown model (IMRPHENOMD) [34] (*bottom row*) for 2×10^5 random spinning, nonprecessing BBHs with 4 $M_\odot \leq M \leq 200\ M_\odot$ using the Advanced LIGO O1 noise PSD and a low-frequency cutoff of 25 Hz. Here $\chi_{\rm eff} \equiv (m_1\chi_1 + m_2\chi_2)/M$ and $\chi_{\rm A} \equiv (\chi_1 - \chi_2)/2$. Points with faithfulness above 97% are not shown. Points with faithfulness $\leq 73\%$ are in red. We note that the biggest changes introduced by the new calibration occur for large, positive $\chi_{\rm eff}$ and positive $\chi_{\rm A}$. The new EOBNR model is most different from the phenomenological model in the large-q, large-$\chi_{\rm eff}$ region, where both models are extrapolated away from the available NR simulations.

simulations in this region are more challenging since the large mass ratio implies the presence of very different scales to be resolved, while the large spin makes the geometry around the BH more difficult to track. As a consequence, very few NR waveforms are available in this region to calibrate the models, and those that have been produced so far [42] are shorter than simulations in less challenging regions of parameter space. As we argue below, more NR waveforms, and most crucially *longer* ones, will be needed in the future to reduce the discrepancy between models in this region and control the systematic error introduced by mismodeling in GW data analysis.

For a more detailed discussion of the faithfulness of SEOBNRv4 against IMRPHENOMD, see Appendix D.

Finally, the top row of Fig. 6 shows the effectualness of the SEOBNRv4 model against a SEOBNRv2 template bank [5] covering total masses 4 $M_\odot \leq M \leq 100\ M_\odot$—as in the O1 run of Advanced LIGO—with a lower frequency cutoff at 25 Hz. SEOBNRv4 injections are drawn with the same distribution as for the faithfulness comparison described above. The effectualness is below 97% only for 3.5% of the overall injection set, implying that the improvements in the SEOBNRv4 model are not crucial for detecting BBH signals, although they are certainly important to extract the correct

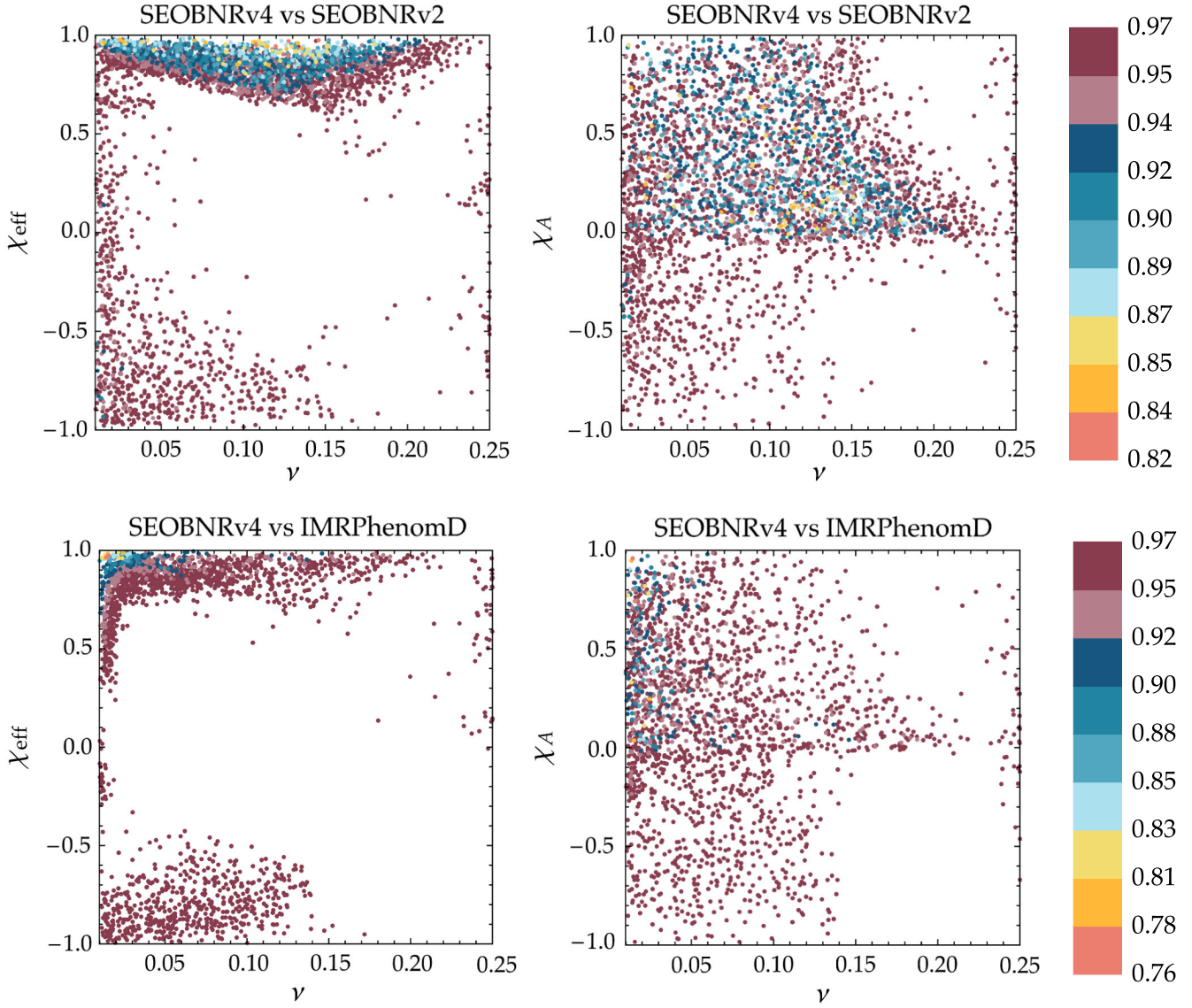

FIG. 6. Effectualness of the EOBNR model of this paper (SEOBNRv4) against the previous EOBNR model (SEOBNRv4) [7] (*top row*) and the phenomenological inspiral-merger-ringdown model (IMRPHENOMD) [34] (*bottom row*): we use 10^5 random spinning, nonprecessing SEOBNRv4 injections 4 $M_\odot \leq M \leq 100\ M_\odot$ that we recover using either a SEOBNRv2 (*top row*) or an IMRPHENOMD (*bottom row*) template bank [5]. Calculations are performed with the Advanced LIGO O1 noise PSD and a low-frequency cutoff of 25 Hz. Here $\chi_{\rm eff} \equiv (m_1\chi_1 + m_2\chi_2)/M$ and $\chi_{\rm A} \equiv (\chi_1 - \chi_2)/2$. Points with effectualness above 97% are not shown. The difference between the models is only present at very large values of $\chi_{\rm eff}$.

BBH parameters upon detection. Consistently with the faithfulness study, the effectualness is smaller in the region of unequal-mass BBHs with very large, positive $\chi_{\rm eff}$ ($\chi_{\rm eff} \gtrsim 0.8$) and positive $\chi_{\rm A}$. The bottom row of Fig. 6 shows the same effectualness computation, but now against an IMRPHENOMD template bank. Here the fraction of points with effectualness below 97% is 2.1%. Points with effectualness below 90% are only 0.06% and are concentrated in the upper left corner of the $(\nu, \chi_{\rm eff})$ plane, that is in the domain of extrapolation for both models, away from the bulk of available NR simulations. The remarkable agreement throughout the vast majority of parameter space is a welcome result. At mass ratios $q \lesssim 8$—at least for a noise configuration similar to that of O1—differences between the two models are comparable to or smaller than the tolerance of template banks construction. We repeated the effectualness computation using the design zero-detuned high-power PSD [109] with a lower frequency cutoff of 15 Hz, finding similar results. Thus, template banks built with either SEOBNRv4 or IMRPHENOMD will not be significantly affected by further improvements in either model in this region. By contrast, reducing the large ineffectualness seen at large mass ratios and large aligned-spin components will require future NR simulations of sufficient length, as we argue in the next section.

VI. LENGTH REQUIREMENTS ON NUMERICAL-RELATIVITY SIMULATIONS FOR CALIBRATION PURPOSES

In Sec. IV D, we have discussed the performance of our model against 141 NR waveforms that were used for its calibration and 5 additional waveforms used for validation, and found agreement to better than 1% in unfaithfulness. It is however important to keep in mind that such a comparison only informs us on the accuracy of the model at frequencies larger than the initial frequency of each NR simulation.[3] In this section, we investigate to what extent our calibration procedure is sufficient to constrain the entire waveform, including the low-frequency portion not covered by NR simulations. Since no direct comparison with NR (or any other surrogate to general relativity whose error is under control) can be performed there, we have to resort to internal consistency checks to identify regions where the calibration procedure becomes unreliable.

In particular, we focus on the following question: can different sets of calibration parameters $\boldsymbol{\theta}$ allow us to faithfully reproduce a given NR waveform, but lead to very different low-frequency behavior? The MCMC infrastructure developed for the calibration makes it easy to address this question, as it provides us with a whole distribution of $\boldsymbol{\theta}$'s for which the EOBNR model closely reproduces NR, on a waveform-per-waveform basis. For definiteness, for each NR configuration we restrict ourselves to those $\boldsymbol{\theta}$'s in the chain for which the unfaithfulness with NR is smaller than 1% across the whole mass range *and* the difference in time of merger (after low-frequency phase alignment) is smaller than $5M$, and randomly draw $N = 1000$ points from that set. In order to understand how these N different EOBNR waveforms differ at low frequency (without having to perform $\mathcal{O}(N^2)$ faithfulness computations), we compare them to a reference waveform corresponding to the set of calibration parameters $\langle\boldsymbol{\theta}\rangle$ defined in the last paragraph of Sec. IV B. We use here a lower frequency cutoff of 25 Hz and the Advanced LIGO design zero-detuned high-power noise PSD curve [109]. In Fig. 7, for each BBH configuration $\boldsymbol{\lambda}$ for which we had a NR run for calibration, we compute the average (over our set of N points) unfaithfulness $1/N\sum_{i=1}^{N}(1 - \langle h_{\rm EOB}(\boldsymbol{\lambda};\langle\boldsymbol{\theta}\rangle)|h_{\rm EOB}(\boldsymbol{\lambda};\boldsymbol{\theta}_i)\rangle)$ as a function of the total mass.

The variability in the low-frequency behavior across the $\boldsymbol{\theta}_i$'s obviously depends on the length of each NR waveform, as well as on the physical parameters $\boldsymbol{\lambda}$. For almost all cases, we find an average faithfulness well below the 1% level, with a worst value very close to this threshold. We therefore conclude that those NR waveforms are long enough to constrain the low-frequency content as well: all sets of calibration parameters that allow to reproduce the NR portion give very similar inspirals from 25 Hz. For some short SXS runs with $q = 1.8$ or 2 (indicated in the legend of Fig. 7, of approximate length $N_{\rm GW\ cycles} = 26$, 26, 27, 27, 27 from top to bottom), the average mismatch grows above the 1% level as the total mass decreases, indicating that those waveforms alone would be too short to calibrate the model with this accuracy at low masses at those BBH configurations. However, this region of parameter space is covered by many other longer NR runs that do not suffer from the same issue, thus we argue that the final model is not affected by this. By contrast, with the more isolated $(q,\chi_1,\chi_2) = (8, 0.85, 0.85)$ NR waveform (see Fig. 1) which contains approximately 15 GW cycles before merger, the average mismatch exceeds 10% at low masses and can be as high as 50% in certain cases. Here, the NR waveform is too short to fully constrain the calibration parameters and our procedure can only ensure that the high-frequency part of the model is correct.

Naturally, the limitations due to the finite length of NR waveforms are not specific to the calibration of the SEOBNRv4 model, and will affect the construction of any inspiral-merger-ringdown model. As an illustration, we discuss the case of the IMRPHENOMD model, which calibrates its phenomenological ansatz to NR waveforms hybridized with

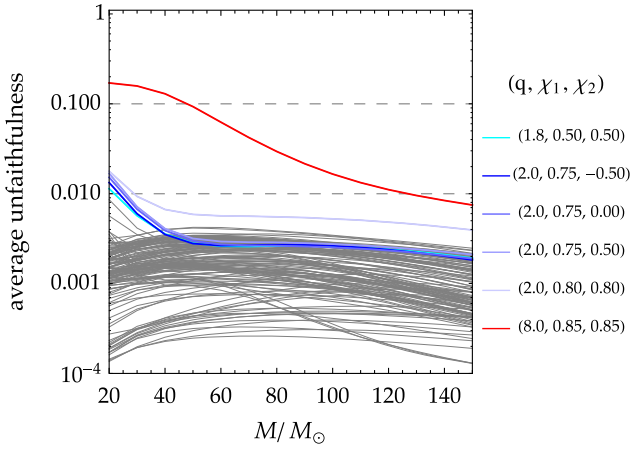

FIG. 7. Convergence of low-frequency EOBNR waveforms upon calibration to NR. For each BBH configuration used in the calibration, we compute the average unfaithfulness between $N = 1000$ EOBNR waveforms generated for values of the calibration parameters $\boldsymbol{\theta}$ that belong to regions of the MCMC posteriors where our calibration requirements (see Sec. IV A) are met and the fiducial EOBNR waveform with calibration parameters $\langle\boldsymbol{\theta}\rangle_{(n)}$. The matches employ a low-frequency cutoff of 25 Hz and the Advanced LIGO design zero-detuned high-power noise PSD. The vast majority of BBHs have average unfaithfulness below 1%, indicating that the current length of NR simulations of those configurations is sufficient to constrain the low-frequency portion of the EOBNR model. On the other hand, for the few cases listed in the legend, the calibration to NR has not lead to convergence of the model at low frequencies, and longer NR simulations are necessary.

[3]We remind the reader that in Fig. 2, the match integral is computed using a lower frequency cutoff corresponding to the fixed initial geometric frequency of the NR waveform.

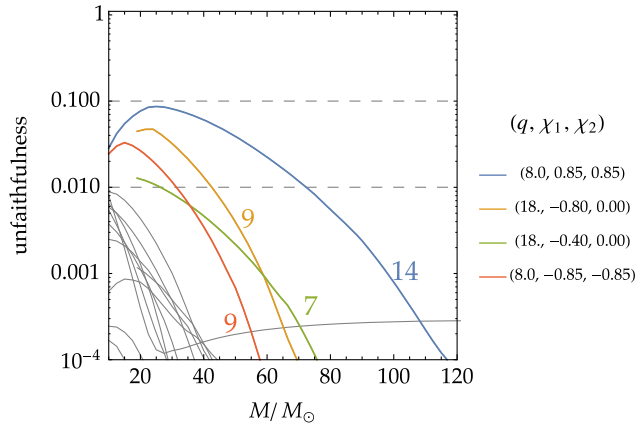

FIG. 8. Impact of NR length on hybrid waveforms used for IMRPHENOMD model [34] calibration. For the BBH configurations that were employed in the calibration of IMRPHENOMD model, we hybridize high-frequency SEOBNRv4 waveforms with low-frequency uncalibrated EOB waveforms at the frequency reported in Table I of Ref. [34]. We then compare these hybrid waveforms to purely SEOBNRv4 waveforms by computing faithfulness from 25 Hz with the Advanced LIGO design zero-detuned high-power noise PSD. The number of GW cycles between the hybridization frequency and the merger is shown next to the 4 curves highlighted in the legend.

an *uncalibrated* version[4] of the EOBNR model. While at sufficiently low frequencies both the calibrated and the uncalibrated model should agree (between themselves and with any PN approximant), they become different in the late inspiral (as soon as the EOB calibration starts to play a role). The use of uncalibrated EOB as an inspiral approximant is justified as long as this difference kicks in after the hybridization frequency. In order to investigate whether this is the case, we build hybrids between the calibrated model (for the high-frequency part, as a surrogate for the actual NR waveforms used in the IMRPHENOMD construction, which are not public) and the uncalibrated one (at low frequencies), and compare them to the calibrated model. We focus on the configurations actually used in the IMRPHENOMD construction, which are listed in Table I of Ref. [34], together with the respective hybridization frequencies.[5] The results are reported in Fig. 8. For most cases, using the uncalibrated EOB model below the hybridization frequency instead of the calibrated one only introduces a mismatch smaller than 1%, even at low masses. In a few cases however, the difference is well above that threshold, indicating that the hybridization frequency is too high—or, equivalently, that the NR waveform actually used in the construction is too short—for the uncalibrated EOB model to still be a good approximant. This is for instance the case for the $(q, \chi_1, \chi_2) = (8, 0.85, 0.85)$ BAM waveform (the same used in this paper). The number of cycles (predicetd by SEOBNRv4) between the hybridization frequency and the merger is approximately $N_{\mathrm{GW\ cycles}} = 14$, 9, 7, 9 from top to bottom for the cases highlighted in the legend.

VII. CONSTRUCTION OF THE REDUCED-ORDER MODEL

The generation of stochastic template banks and Bayesian parameter-estimation simulations require on the order of 10^6–10^8 waveform evaluations. Since the numerical integration of the EOB orbital dynamics through Hamilton's equations and the generation of gravitational waveforms can take from seconds to hours, depending on the binary's parameters, it can be quite slow to produce EOBNR waveforms for data-analysis applications.

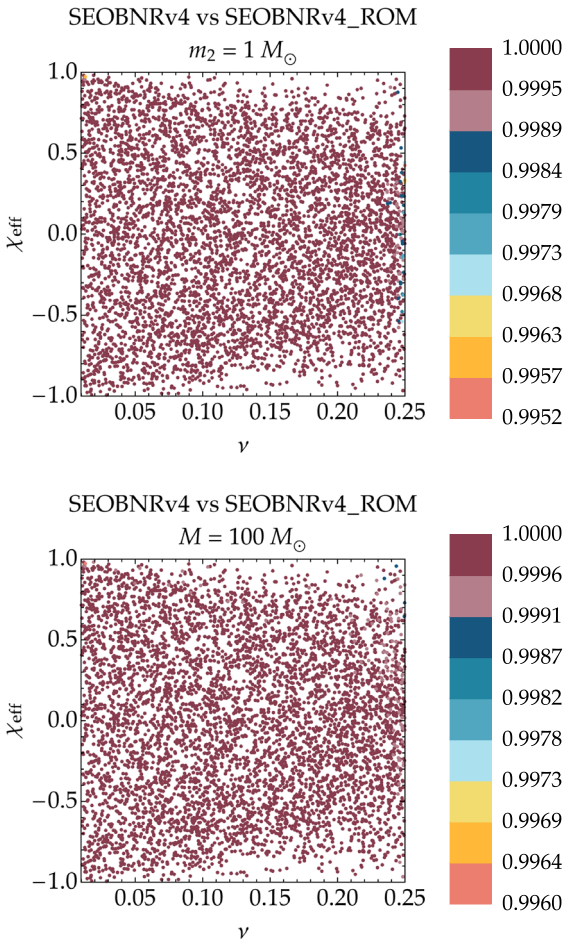

FIG. 9. Faithfulness of the SEOBNRv4_ROM model against SEOBNRv4 model as a function of the symmetric mass ratio ν and the effective spin combination χ_{eff}. The aLIGO O1 PSD [116] is used with a low frequency cutoff of 20 Hz. The top panel shows unfaithfulness for BBHs where the smaller body is fixed at 1 $M_\odot$, while in the bottom panel the total mass is fixed at 100 $M_\odot$.

[4]An important motivation behind this choice is to avoid calibrating models against each other, an independence which is crucial in order to estimate systematic errors introduced by modeling by comparing two models as done in Ref. [28]).

[5]Note that the frequency reported for the $(q, \chi_1, \chi_2) = (8, 0.85, 0.85)$ waveform is incorrect and should read $Mf_{\mathrm{hyb}} = 0.0175$.

Reduced order modeling (ROM) allows for the construction of fast and accurate surrogates of waveform models. ROMs combine methods for building reduced bases of waveforms (or their amplitudes and phasings) and interpolation techniques of expansion coefficients over the binary's parameter space. Established methods use singular-value decomposition (SVD) with tensor product spline interpolation [8,117–120] or the greedy-basis algorithm and empirical interpolation method [121–124]. Previous work on ROMs for EOBNR models [8,117] has demonstrated speed-ups to up to several thousands with ROM errors smaller than the EOBNR's calibration errors, that is ∼1%.

In this study, we follow the ROM construction described in Refs. [8] and [117]. The Fourier-domain amplitude and phase of SEOBNRv4 input waveforms are interpolated onto a sparse, geometric frequency grid spanning $[9.85 \times 10^{-5}, 0.3]$. The ringdown is extended by fitting the amplitude of all input waveforms to an exponentially damped Lorentzian function. We use patching in the frequency domain and over the parameter space as introduced in Ref. [8]. It is efficient to split the construction into low and high frequency ROMs. At low frequencies the ROM needs to capture the early inspiral part of the waveform, which varies smoothly and only requires moderate resolution over the parameter space, while finer structure from the merger and ringdown must be resolved at high frequencies with a finer grid of input waveforms. In addition, resolution requirements are not uniform over the parameter space. Since tensor product interpolation does not allow for local refinement regions we switch between multiple overlapping patches which provide a covering of the mass-ratio and aligned spin space.

A single low-frequency patch is joined with two high-frequency patches at a frequency $Mf_{\rm m} = 0.01$. The low-frequency patch uses a grid of $70 \times 12 \times 12$ waveforms in $\{\nu, \chi_1, \chi_2\}$ with 259 sparse frequency points. It spans the domain of the Cartesian product of intervals $0.01 \leq \nu \leq 0.25$ and $-1 \leq \chi_{1,2} \leq 1$. The first high-frequency patch spans this same domain on a grid of $57 \times 33 \times 21$ waveforms with 149 frequency points. This is complemented by a second high-frequency patch covering the domain with $0.01 \leq \nu \leq 0.025$, $0.995 \leq \chi_1 \leq 1$, and $-1 \leq \chi_2 \leq 1$ on a grid of $13 \times 11 \times 21$ waveforms and 325 frequency points to provide higher resolution for the merger-ringdown part of the waveforms. Outside the domain of the second high-frequency patch, the first high-frequency patch is used.

In Fig. 9 we show the faithfulness of the SEOBNRv4_ROM model against the SEOBNRv4_ model for the aLIGO O1 PSD [116] with a low-frequency cutoff of 20 Hz. We find that, overall, the SEOBNRv4_ROM model is accurate to better than 1% in unfaithfulness for BBHs with a total mass of $2\ M_\odot$ or higher. For low masses, the unfaithfulness in the bulk is lower than 0.1%, except for some configurations near equal mass where it can rise to 0.4%. For total masses of $M = 100\ M_\odot$ the unfaithfulness is again lower than 0.1% and slightly above that in the very high mass-ratio—spin corner of the parameter space. The unfaithfulness rises to 0.4% for $M = 300\ M_\odot$. For total masses higher than about $500\ M_\odot$ differences between the ringdown description in the ROM and SEOBNRv4 can result in unfaithfulness above 1% for some configurations.

In Fig. 10 we show the speed-up of the SEOBNRv4_ROM model against the SEOBNRv4 model and the SEOBNRv4_OPT model, which is a version of the SEOBNRv4 code with significant optimizations [125]. We see that the SEOBNRv4_ROM model is several thousand times faster than the SEOBNRv4 model and a factor 20–50 faster than the SEOBNRv4_OPT model.

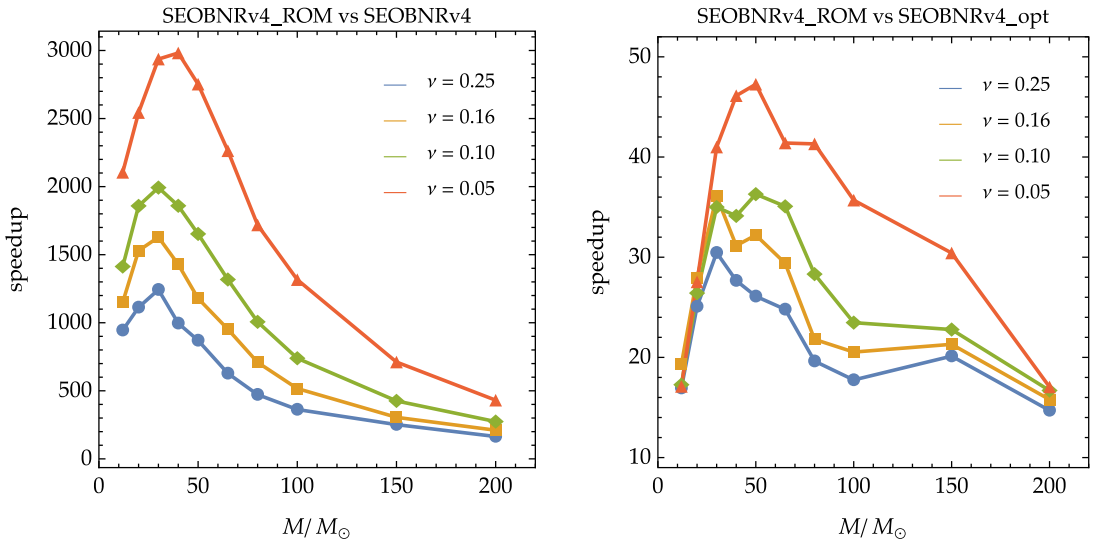

FIG. 10. Speedup of the SEOBNRv4_ROM model compared to SEOBNRv4 (*left panel*) and SEOBNRv4_OPT (*right panel*) models as a function of the total mass for several mass ratios.

VIII. CONCLUSIONS

We built a new, calibrated EOBNR waveform model for spinning, nonprecessing BBHs (SEOBNRv4) using 12 BH-perturbation-theory waveforms [57] and 141 NR simulations [38–42,66], which extend to larger positive aligned-spin components and more spin-asymmetric configurations as compared to the NR waveforms employed in the previous version of the EOBNR model [7]. After calibrating the model, interpolating and extrapolating it to arbitrary mass ratios and spins, we found that the model can reproduce the NR waveforms with a faithfulness larger than 99% using the Advanced LIGO design zero-detuned high-power noise PSD [109] for total masses $10\,M_\odot \leq M \leq 200\,M_\odot$. This also holds true for 6 new NR simulations that were produced for this paper but were not used in the calibration and 10 NR waveforms that were employed for validation. To achieve this level of accuracy, we employed MCMC techniques to explore the 4D space of inspiral-plunge calibration parameters and we employed phenomenological fitting formulas for the ringdown signal.

We compared the improved EOBNR model to spinning, nonprecessing waveform models that were used in the data analysis of the O1 run of Advanced LIGO, namely SEOBNRv2 [7] and IMRPHENOMD [34]. We carried out faithfulness comparisons from 25 Hz with the O1 noise PSD [116]. We found that SEOBNRv4 has faithfulness[6]: (i) as low as 43% against SEOBNRv2 in the region of large, positive aligned-spin components and spin-asymmetric BBHs, irrespective of the mass ratio, where new NR simulations became available for calibration; (ii) as low as 35% against IMRPHENOMD in the region of large, positive aligned-spin components and large mass ratios, where both models are extrapolating away from the respective calibration domain and the number of GW cycles in band is larger than in any other part of parameter space. We note that the fraction of points with faithfulness below 97% is only about 8% (7%) of the total when comparing SEOBNRv4 to SEOBNRv2 (IMRPHENOMD). The faithfulness results against IMRPHENOMD waveforms at mass ratios $\gtrsim 4$ and aligned-spin components $\gtrsim 0.8$ strongly suggest the importance of producing new NR simulations in this region of the parameter space, so that discrepancies between different ways of extrapolating waveform models can be resolved. By contrast, the high effectualness between SEOBNRv4 and IMRPHENOMD waveform models in almost all parameter space (both for O1 and design noise curves), suggests that for Advanced LIGO detection purposes the dominant-mode models do not need to be further improved. However, the inclusion of higher modes is likely to be important to increase our chance of detecting binary coalescences in some regions of the parameter space [126], notably large mass ratios.

Several studies were carried out in the past to try to understand how to build semianalytic waveform models tuned and/or hybridized to NR waveforms, so that they could be trusted outside the frequency region (or mass range) in which the NR information is employed (e.g., see Refs. [127–129] and references therein). Here, we assessed how much the finite length of available NR simulations affects the calibration of inspiral-merger-ringdown models. We showed that, for a handful of BBH configurations in the NR catalog at our disposal, the calibration cannot yet constrain the low-frequency portion of the model due to the small length of the NR runs. We restricted the scope of this study to flagging points at which longer NR waveforms are required. A more ambitious study would consist in trying to predict the initial NR frequency necessary to satisfactorily constrain the low frequencies in the model *at points in parameter space where we do not have long enough waveforms yet*. As a first step, one would need to determine for each NR waveform available the largest frequency for which the low frequencies are well constrained (say for which the average faithfulness is smaller than 1% for all masses). This requires running several MCMC chains where the NR waveform is artificially cut at increasingly large initial frequencies. Once this minimal frequency requirement has been identified for each available waveform, one could then try to extrapolate to other values of (q,χ_1,χ_2). Given its expensive character, such a study is however beyond the scope of this paper and we reserve it for future work. We also showed that the construction of hybrids using uncalibrated EOB waveforms in the low-frequency regime (as done in IMRPHENOMD) can be problematic when the hybridization frequency is too high.

We have shown the importance of new, long NR waveforms with both high mass ratio and high spin, but this region of the parameter space was challenging for SPEC. As a result, we have made use of an existing (short) waveform from BAM for calibration, and new (short) waveforms that we produced using the EINSTEIN TOOLKIT for validation. Each code has different strengths, and combining results from all three allows the best possible science to be performed.

We plan to trade the spinning, nonprecessing dynamics and waveforms of the precessing EOBNR model of Refs. [23,26] with the improved version developed in this paper, so that the 15-dimensional fully precessing EOBNR model can infer more accurately the properties [28,29] of future detections of coalescing binaries with Advanced LIGO.

Finally, we built a reduced-order model of SEOBNRv4 that can be orders of magnitude faster than its time-domain implementation in generating waveforms, while still being faithful to it for data-analysis applications in Advanced LIGO.

[6]We notice that the regions of low faithfulness are far from the parameter space where GW150914 and GW151226 were observed.

The model described in this paper, as well as its ROM version, has already been implemented and reviewed in LAL [36], and is publicly available under the name of SEOBNRv4 and SEOBNRv4_ROM, respectively.

ACKNOWLEDGMENTS

We would like to thank Mark Hannam and Sascha Husa for kindly providing us with the nonpublic BAM $(q,\chi_1,\chi_2) = (8, 0.85, 0.85)$ waveform, which was used in Sec. IV to calibrate the EOB model. This work was supported in part at Caltech by the Sherman Fairchild Foundation and NSF Grants No. PHY-1404569, at Cornell by NSF Grants No. PHY-1606654 and No. AST-1333129 and the Sherman Fairchild Foundation and at Cal State Fullerton by NSF grants PHY-1307489 and PHY-1606522. We gratefully acknowledge support for this research at CITA from NSERC of Canada, the Ontario Early Researcher Awards Program, the Canada Research Chairs Program, and the Canadian Institute for Advanced Research. Calculations were performed at the GPC supercomputer at the SciNet HPC Consortium; SciNet is funded by: the Canada Foundation for Innovation (CFI) under the auspices of Compute Canada; the Government of Ontario; Ontario Research Fund (ORF)—Research Excellence; and the University of Toronto. Further calculations were performed on the Briarée cluster at Sherbrooke University, managed by Calcul Québec and Compute Canada and with operation funded by the Canada Foundation for Innovation (CFI), Ministère de l'Économie, de l'Innovation et des Exportations du Quebec (MEIE), RMGA and the Fonds de recherche du Québec–Nature et Technologies (FRQ-NT). Some of the calculations were performed on the ORCA cluster at Cal State Fullerton, which is supported by the Research Corporation for Science Advancement, PHY-1429873, and Cal State Fullerton. New NR simulations were performed on the AEI Datura and Minerva clusters. The Markov-chain Monte Carlo runs were performed on the AEI Vulcan cluster.

APPENDIX A: INPUT VALUES FOR THE DOMINANT-MODE MERGER WAVEFORM

In this Appendix we provide fitting formulas for the values of amplitude, curvature of the amplitude, GW frequency, and slope of the GW frequency of the (2,2) mode at the peak of radiation.

Let $f(\nu,\chi)$ denote any such fit. First, we extract the input values from both the NR and the test-particle Teukolsky-code waveforms used in this paper (see Sec. III). Let us now focus on how to build fits for peak amplitude, curvature of the amplitude, and slope of the GW frequency; we will discuss the case of the peak frequency later. The fits for these three quantities are built as follows: (i) We fit the Teukolsky data as a function of χ at fixed $\nu = 10^{-3}$ (test-particle limit) with a suitable function $f_{\rm TPL}(\chi)$; (ii) We fit the NR data as a function of χ at fixed $\nu = 1/4$ (equal-mass limit) with a suitable function $f_{\rm EQ}(\chi)$; (iii) We assume a polynomial dependence in ν and impose that $f(\nu = 10^{-3},\chi) = f_{\rm TPL}(\chi)$ and $f(\nu = 1/4,\chi) = f_{\rm EQ}(\chi)$: this fixes two coefficients in the polynomial expansion; (iv) The rest of the coefficients are determined through a global fit over the whole (ν,χ) parameter space where we have NR data. For the peak GW frequency we build test-particle-limit and equal-mass-limit fits as in (i) and (ii), but then we prescribe a linear dependence on ν for the global fit.

1. Amplitude at the peak

The test-particle-limit and equal mass (Z = TPL or EQ) fit read

$$f_{\rm Z}(\chi)/\nu = \sum_{i=0}^{3} p_i^{(\rm Z)}\chi^i, \tag{A1}$$

with

$$p_0^{(\rm TPL)} = 1.452857, \qquad p_0^{(\rm EQ)} = 1.577458,$$
$$p_1^{(\rm TPL)} = 0.166134, \qquad p_1^{(\rm EQ)} = -0.007695,$$
$$p_2^{(\rm TPL)} = 0.027356, \qquad p_2^{(\rm EQ)} = 0.021887,$$
$$p_3^{(\rm TPL)} = -0.020073, \qquad p_3^{(\rm EQ)} = 0.023268.$$

The global fit reads

$$f(\nu,\chi)/\nu = \sum_{i=0}^{2} A_i\nu^i, \tag{A2}$$

where A_0 and A_2 are fixed by requiring that the test-particle-limit and equal-mass-limit fits are recovered exactly when $\nu = 10^{-3}$ and $\nu = 1/4$, respectively, and $A_1 = \sum_{k=0}^{3} e_k\chi^k$, with

$$e_0 = -0.034424, \qquad e_1 = -1.218066,$$
$$e_2 = -0.568373, \qquad e_3 = 0.401114.$$

2. Curvature of amplitude at the peak

The test-particle-limit and equal mass fit read

$$f_{\rm TPL}(\chi)/\nu = \sum_{i=1}^{3} p_i^{(\rm TPL)}(\chi - 1)^i, \tag{A3}$$

$$f_{\rm EQ}(\chi)/\nu = \sum_{i=0}^{1} p_i^{(\rm EQ)}\chi^i, \tag{A4}$$

with

$$p_1^{(\rm TPL)} = 0.00239561, \qquad p_0^{(\rm EQ)} = -0.00412651,$$
$$p_2^{(\rm TPL)} = -0.00019274, \qquad p_1^{(\rm EQ)} = 0.00222400.$$
$$p_3^{(\rm TPL)} = -0.00029666.$$

The global fit reads

$$f(\nu,\chi)/\nu = \sum_{i=0}^{2} A_i \nu^i, \tag{A5}$$

where A_0 and A_2 are fixed by requiring that the test-particle-limit and equal-mass-limit fits are recovered exactly when $\nu = 10^{-3}$ and $\nu = 1/4$, respectively, and $A_1 = \sum_{k=0}^{1} e_k \chi^k$, with

$$e_0 = -0.00577654, \qquad e_1 = 0.00103086.$$

3. GW frequency at the peak

The test-particle-limit fit reads

$$f_{\rm TPL}(\chi) = p_0^{\rm (TPL)} + (p_1^{\rm (TPL)} + p_2^{\rm (TPL)}\chi) \times \log(p_3^{\rm (TPL)} - p_4^{\rm (TPL)}\chi), \tag{A6}$$

with

$$p_0^{\rm (TPL)} = 0.562679, \qquad p_1^{\rm (TPL)} = -0.087062,$$
$$p_2^{\rm (TPL)} = 0.001743, \qquad p_3^{\rm (TPL)} = 25.850378,$$
$$p_4^{\rm (TPL)} = 25.819795.$$

The equal-mass-limit fit reads

$$f_{\rm EQ}(\chi) = p_0^{\rm (TPL)} + (p_1^{\rm (TPL)} + p_2^{\rm (TPL)}\chi) \times \log(p_3^{\rm (EQ)} - p_4^{\rm (EQ)}\chi), \tag{A7}$$

with

$$p_3^{\rm (EQ)} = 10.262073, \qquad p_4^{\rm (EQ)} = 7.629922.$$

The global fit reads

$$f(\nu,\chi) = p_0^{\rm (TPL)} + (p_1^{\rm (TPL)} + p_2^{\rm (TPL)}\chi)\log(A_3 - A_4\chi), \tag{A8}$$

with

$$A_3 = p_3^{\rm (EQ)} + 4(p_3^{\rm (EQ)} - p_3^{\rm (TPL)})(\nu - 1/4),$$
$$A_4 = p_4^{\rm (EQ)} + 4(p_4^{\rm (EQ)} - p_4^{\rm (TPL)})(\nu - 1/4). \tag{A9}$$

4. Slope of GW frequency at the peak

The test-particle-limit fit reads

$$f_{\rm TPL}(\chi) = p_0^{\rm (TPL)} + (p_1^{\rm (TPL)} + p_2^{\rm (TPL)}\chi) \times \log(p_3^{\rm (TPL)} - p_4^{\rm (TPL)}\chi), \tag{A10}$$

with

$$p_0^{\rm (TPL)} = -0.011210, \qquad p_1^{\rm (TPL)} = 0.004087,$$
$$p_2^{\rm (TPL)} = 0.000633, \qquad p_3^{\rm (TPL)} = 68.474666,$$
$$p_4^{\rm (TPL)} = 58.301488.$$

The equal-mass-limit fit reads

$$f_{\rm EQ}(\chi) = \sum_{i=0}^{1} p_i^{\rm (EQ)} \chi^i, \tag{A11}$$

with

$$p_0^{\rm (EQ)} = 0.011282, \qquad p_1^{\rm (EQ)} = 0.000287.$$

The global fit reads

$$f(\nu,\chi) = \sum_{i=0}^{2} A_i \nu^i, \tag{A12}$$

where A_0 and A_2 are fixed by requiring that the test-particle-limit and equal-mass-limit fits are recovered exactly when $\nu = 10^{-3}$ and $\nu = 1/4$, respectively, and $A_1 = \sum_{k=0}^{1} e_k \chi^k$, with

$$e_0 = 0.015743, \qquad e_1 = 0.022442.$$

APPENDIX B: PHENOMENOLOGICAL MERGER-RINGDOWN MODEL

Here, we discuss the performance of our phenomenological merger-ringdown model (see Sec. II C), which builds on previous work [59–61], and we also compare it to the model of Ref. [61]. In order to more easily describe the comparison that we perform, we first summarize some similarities and differences between the two models.

The model of Ref. [61] is a complete model of the post-merger phase in that it also specifies initial conditions at the time of merger: the value of the amplitude (its first derivative is 0 by construction) and of the frequency at that point are prescribed by fits (functions of ν and the spin combination $a_0 = (m_1\chi_1 + m_2\chi_2)/M$ (see the last two rows of Table 1 in Ref. [61]). By contrast, the model presented in Sec. II C attaches a ringdown portion to any inspiral-plunge waveform by imposing a C^1 behavior at the attachment point (assumed to be the amplitude's peak). However, in the context of the EOBNR model developed in this paper (SEOBNRv4), the values of the amplitude and the frequency at the attachment point are imposed by the explicit expressions (fits to NR) given in Appendix A. We can therefore obtain a full model of the post-merger phase by simply combining the information in Sec. II C and in Appendix A.

Both models make use of a phenomenological ansatz where the dominant QNM is factored out. In our EOBNR model, the value of the dominant (complex) QNM frequency is obtained by first computing the mass and spin of the remnant object from the fitting formulae in Refs. [7,65] (which were calibrated using hundreds of publicly available

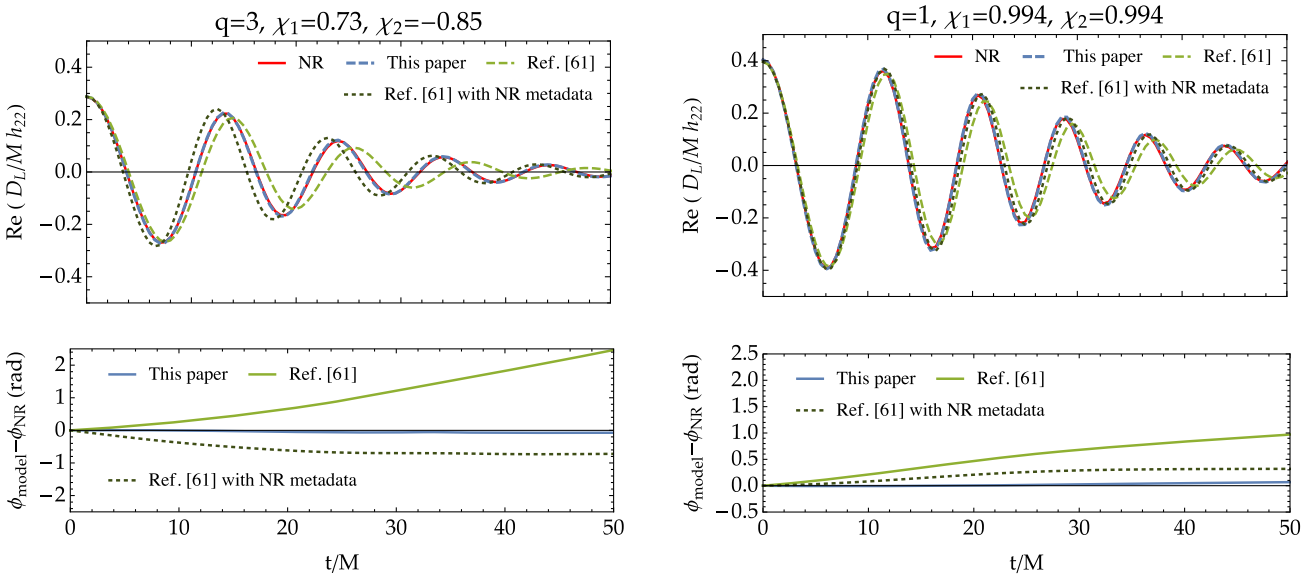

FIG. 11. Waveform comparison in the time-domain between the merger-ringdown models of this paper and of Ref. [61] and NR for two configurations in our NR catalog. The one in the left panel $(q,\chi_1,\chi_2)=(3,0.73,-0.85)$ was used in the calibration of the SEOBNRv4 model only. The one in the right panel, $(q,\chi_1,\chi_2)=(1,0.994,0.994)$ entered the calibration of both models. Phases are aligned at $t=0$ which corresponds to the amplitude peak. The top plots show the real part of each waveform while the bottom plots show the phase difference between the models and NR. The green line corresponds to the purely stand-alone model described in Ref. [61] whereas the dotted line labeled Ref. [61] "+NR metadata" corresponds to the same model but with the QNM determined using the NR metadata for the remnant properties and the tables in Ref. [62] instead of using the fits in Table I of Ref. [61].

NR waveforms) and then interpolating results from Ref. [62]. By contrast, Ref. [61] directly provides fits allowing us to reconstruct the real and imaginary part of the QNM as functions of ν and a_0.[7] The authors of Ref. [61] however informed us [130] that the comparisons to NR that are shown in their paper do not use those fits to reconstruct the QNM. Instead, for each NR waveform against which their model is compared, the mass and spin of the remnant BH is read from the NR metadata and used together with the tables in Ref. [62] to determine the QNM. This leads to an improved behavior as the real part of the QNM, a crucial ingredient of the model, is determined much more precisely than using the fits. However, such a procedure can only be applied at points in parameter space where an NR waveform exists and cannot be considered as part of a final stand-alone analytical model. In Fig. 11, we show the performance using both implementations. We expect that using the same tools as the ones in our model (very accurate fits existing in the literature for the remnant properties and interpolation of the tables in Ref. [62]) to determine the QNM will lead to an intermediate performance, likely closer to using the NR metadata.

Given a set of physical parameters (m_1,m_2,χ_1,χ_2) for the binary components, our model provides a complete prescription for the ringdown waveform (by which we mean the portion of waveform starting at the amplitude peak of the full signal). For the model of Ref. [61], we additionally need the mass of the final BH. Since here we want to compare the models to NR, we know the *exact* value for the final mass for each configuration and use it for the model of Ref. [61]. For our EOBNR model, we keep using the value provided by the fit in Ref. [7]. We can then compare directly to NR (without using any further information from the NR waveform itself). All phases are set to 0 at $t=0$. Two examples are shown in Fig. 11, namely the $(q,\chi_1,\chi_2)=(3,0.73,-0.85)$ configuration (left panel), which was used to calibrate our model but not the model of Ref. [61] and the $(q,\chi_1,\chi_2)=(1,0.994,0.994)$ configuration (right panel), which was used in both models. As we can see, whereas in our merger-ringdown model (i.e., SEOBNRv4), the dephasing remains of the order of 0.1 rad throughout the merger-ringdown phase, in the model of Ref. [61] it grows to more than 1 rad. Using the NR metadata to determine the QNM instead of the fits provided in Table I improves the behavior of the model of Ref. [61] by removing the linear drift of the phase, since the ringdown frequency is now exactly known. Even using this additional information coming from NR, the asymptotic dephasing reaches several tenths of radians.

Going beyond this time-domain comparison, we can also try to quantify the performance of the models in terms of faithfulness. In order to avoid computing matches between

[7]Note that the imaginary part is not directly fitted. Instead, fits for the frequency at merger and for a combination ($\Delta\omega$ in their notation) of the frequency at merger and of the real part of the QNM are given.

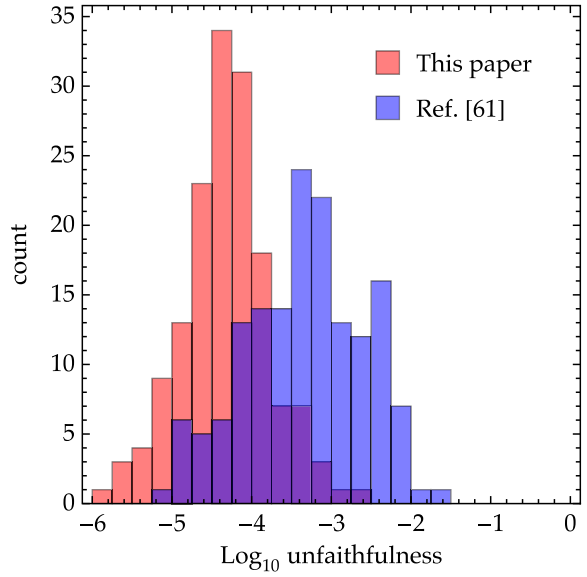

FIG. 12. Comparison of the performance of the merger-ringdown models of this paper and of Ref. [61] over the catalog of 147 NR waveforms used in this paper. For each configuration, the faithfulness of each model to NR is computed at a total mass such that the merger frequency is at 50 Hz.

post-merger waveforms only (which would require tapering the signal at $t = 0$), we attach the post-merger portion predicted by each model to the NR waveform itself cut at the peak. However, there is an obvious problem in doing this. The resulting hybrid waveforms would not even be continuous at the peak since both the fits of Appendix A and the last two rows of Table I of Ref. [61] do not *exactly* reproduce the NR values. For the purpose of this comparison only, we therefore replace the values predicted by the fits in each model by the actual NR values.[8] We then compute the faithfulness between the original NR waveform and the hybrid ones, choosing a total mass M such that the peak of the waveform lies at 50 Hz so that the merger-ringdown is in the most sensitive spot of the detector's noise curve. The distribution of faithfulness obtained across the catalog is shown in Fig. 12. In most cases (all cases for SEOBNRv4), both models lead to negligible unfaithfulness from the point of view of data-analysis applications. The model of Ref. [61] however features a tail extending above the 1% level, mainly composed of waveforms with very antisymmetric spin configurations (such as the one shown in the left panel of Fig. 11) that were not included in the calibration of this model since they were not publicly available at the time. In summary, we find that calibrating our phenomenological expressions for the merger-ringdown part of the model to an extensive NR catalog such as the one used in this paper is crucial to obtain a highly accurate model everywhere in parameter space. New, future NR waveforms will allow us to further test and extend the model.

[8]There is an additional subtlety in doing this in the model of Ref. [61]. The QNM frequency is not directly provided as a fit. Using the NR value for ω_{22} but keeping the fit value for their $\Delta\omega$ leads to a slightly modified value of the dominant QNM frequency. To make sure that the QNM frequency predicted by the model in Ref. [61] is preserved, we first compute it using $\omega_1 = M_{\rm BH}\omega_{22}^{\rm mrg} - \Delta\omega$ where $\omega_{22}^{\rm mrg}$ and $\Delta\omega$ are evaluated using the fits, and then use the NR value for $\omega_{22}^{\rm mrg}$ elsewhere, redefining $\Delta\omega = \omega - M_{\rm BH}\omega_{22}^{\rm NR}$ to ensure continuity at $t = 0$.

APPENDIX C: EXISTING NUMERICAL-RELATIVITY SIMULATIONS USED IN THIS WORK

In addition to the new NR waveforms listed in Table I, we have also used previously-produced waveforms, described in Secs. C 1–C 4. Some waveforms were used only for validation of the model; in this case, they follow the calibration waveforms and are separated by a horizontal line. The table columns are the same as in Table I.

1. SXS waveforms from Ref. [38]

ID	q	χ_1	χ_2	e	$M\omega_{22}$	$N_{\rm orb}$
SXS:BBH:0004	1.0	−0.50	+0.00	3.7×10^{-4}	0.01151	30.2
SXS:BBH:0005	1.0	+0.50	+0.00	2.5×10^{-4}	0.01227	30.2
SXS:BBH:0007	1.5	+0.00	+0.00	4.2×10^{-4}	0.01229	29.1
SXS:BBH:0013	1.5	+0.50	+0.00	1.4×10^{-4}	0.01444	23.8
SXS:BBH:0016	1.5	−0.50	+0.00	4.2×10^{-4}	0.01149	30.7
SXS:BBH:0019	1.5	−0.50	+0.50	7.6×10^{-5}	0.01460	20.4
SXS:BBH:0025	1.5	+0.50	−0.50	7.6×10^{-5}	0.01456	22.4
SXS:BBH:0030	3.0	+0.00	+0.00	2.0×10^{-3}	0.01775	18.2
SXS:BBH:0036	3.0	−0.50	+0.00	5.1×10^{-4}	0.01226	31.7
SXS:BBH:0045	3.0	+0.50	−0.50	6.4×10^{-4}	0.01748	21.0

(Table continued)

(Continued)

ID	q	χ_1	χ_2	e	$M\omega_{22}$	$N_{\rm orb}$
SXS:BBH:0046	3.0	−0.50	−0.50	2.6×10^{-4}	0.01771	14.4
SXS:BBH:0047	3.0	+0.50	+0.50	4.7×10^{-4}	0.01743	22.7
SXS:BBH:0056	5.0	+0.00	+0.00	4.9×10^{-4}	0.01589	28.8
SXS:BBH:0060	5.0	−0.50	+0.00	3.4×10^{-3}	0.01608	23.2
SXS:BBH:0061	5.0	+0.50	+0.00	4.2×10^{-3}	0.01578	34.5
SXS:BBH:0063	8.0	+0.00	+0.00	2.8×10^{-4}	0.01938	25.8
SXS:BBH:0064	8.0	−0.50	+0.00	4.9×10^{-4}	0.01968	19.2
SXS:BBH:0065	8.0	+0.50	+0.00	3.7×10^{-3}	0.01887	34.0
SXS:BBH:0148	1.0	−0.44	−0.44	2.0×10^{-5}	0.01634	15.5
SXS:BBH:0149	1.0	−0.20	−0.20	1.8×10^{-4}	0.01614	17.1
SXS:BBH:0150	1.0	+0.20	+0.20	2.9×10^{-4}	0.01591	19.8
SXS:BBH:0151	1.0	−0.60	−0.60	2.5×10^{-4}	0.01575	14.5
SXS:BBH:0152	1.0	+0.60	+0.60	4.3×10^{-4}	0.01553	22.6
SXS:BBH:0153	1.0	+0.85	+0.85	8.3×10^{-4}	0.01539	24.5
SXS:BBH:0154	1.0	−0.80	−0.80	3.3×10^{-4}	0.01605	13.2
SXS:BBH:0155	1.0	+0.80	+0.80	4.7×10^{-4}	0.01543	24.1
SXS:BBH:0156	1.0	−0.95	−0.95	5.4×10^{-4}	0.01643	12.4
SXS:BBH:0157	1.0	+0.95	+0.95	1.4×10^{-4}	0.01535	25.2
SXS:BBH:0158	1.0	+0.97	+0.97	7.9×10^{-4}	0.01565	25.3
SXS:BBH:0159	1.0	−0.90	−0.90	5.6×10^{-4}	0.01588	12.7
SXS:BBH:0160	1.0	+0.90	+0.90	4.2×10^{-4}	0.01538	24.8
SXS:BBH:0166	6.0	+0.00	+0.00	4.4×10^{-5}	0.01940	21.6
SXS:BBH:0167	4.0	+0.00	+0.00	9.9×10^{-5}	0.02054	15.6
SXS:BBH:0169	2.0	+0.00	+0.00	1.2×10^{-4}	0.01799	15.7
SXS:BBH:0170	1.0	+0.44	+0.44	1.3×10^{-4}	0.00842	15.5
SXS:BBH:0172	1.0	+0.98	+0.98	7.8×10^{-4}	0.01540	25.4
SXS:BBH:0174	3.0	+0.50	+0.00	2.9×10^{-4}	0.01337	35.5
SXS:BBH:0180	1.0	+0.00	+0.00	5.1×10^{-5}	0.01227	28.2

2. SXS waveforms from Ref. [40,41,66]

ID	q	χ_1	χ_2	e	$M\omega_{22}$	$N_{\rm orb}$
SXS:BBH:0177	1.0	+0.99	+0.99	1.3×10^{-3}	0.01543	25.4
SXS:BBH:0178	1.0	+0.99	+0.99	8.6×10^{-4}	0.01570	25.4
SXS:BBH:0202	7.0	+0.60	+0.00	9.0×10^{-5}	0.01324	62.1
SXS:BBH:0203	7.0	+0.40	+0.00	1.4×10^{-5}	0.01322	58.5
SXS:BBH:0204	7.0	+0.40	+0.00	1.7×10^{-4}	0.01044	88.4
SXS:BBH:0205	7.0	−0.40	+0.00	7.0×10^{-5}	0.01325	44.9
SXS:BBH:0206	7.0	−0.40	+0.00	1.6×10^{-4}	0.01037	73.2
SXS:BBH:0207	7.0	−0.60	+0.00	1.7×10^{-4}	0.01423	36.1
SXS:BBH:0306	1.3	+0.96	−0.90	1.5×10^{-3}	0.02098	12.6

3. SXS waveforms from Ref. [39]

ID	q	χ_1	χ_2	e	$M\omega_{22}$	$N_{\rm orb}$
SXS:BBH:0290	3.0	+0.60	+0.40	9.0×10^{-5}	0.01758	24.2
SXS:BBH:0291	3.0	+0.60	+0.60	5.0×10^{-5}	0.01764	24.5

(Table continued)

(Continued)

ID	q	χ_1	χ_2	e	$M\omega_{22}$	$N_{\rm orb}$
SXS:BBH:0289	3.0	+0.60	+0.00	2.3×10^{-4}	0.01711	23.8
SXS:BBH:0285	3.0	+0.40	+0.60	1.6×10^{-4}	0.01732	23.8
SXS:BBH:0261	3.0	−0.73	+0.85	1.0×10^{-4}	0.01490	21.5
SXS:BBH:0293	3.0	+0.85	+0.85	9.0×10^{-5}	0.01813	25.6
SXS:BBH:0280	3.0	+0.27	+0.85	9.7×10^{-5}	0.01707	23.6
SXS:BBH:0257	2.0	+0.85	+0.85	1.1×10^{-4}	0.01633	24.8
SXS:BBH:0279	3.0	+0.23	−0.85	6.0×10^{-5}	0.01629	22.6
SXS:BBH:0274	3.0	−0.23	+0.85	1.6×10^{-4}	0.01603	22.4
SXS:BBH:0258	2.0	+0.87	−0.85	1.8×10^{-4}	0.01612	22.8
SXS:BBH:0248	2.0	+0.13	+0.85	7.0×10^{-5}	0.01552	23.2
SXS:BBH:0232	1.0	+0.90	+0.50	2.8×10^{-4}	0.01558	23.9
SXS:BBH:0229	1.0	+0.65	+0.25	3.1×10^{-4}	0.01488	23.1
SXS:BBH:0231	1.0	+0.90	+0.00	1.0×10^{-4}	0.01487	23.1
SXS:BBH:0239	2.0	−0.37	+0.85	9.1×10^{-5}	0.01478	22.2
SXS:BBH:0252	2.0	+0.37	−0.85	3.8×10^{-4}	0.01488	22.5
SXS:BBH:0219	1.0	−0.50	+0.90	3.3×10^{-4}	0.01484	22.4
SXS:BBH:0211	1.0	−0.90	+0.90	2.6×10^{-4}	0.01411	22.3
SXS:BBH:0233	2.0	−0.87	+0.85	6.0×10^{-5}	0.01423	22.0
SXS:BBH:0243	2.0	−0.13	−0.85	1.8×10^{-4}	0.01378	23.3
SXS:BBH:0214	1.0	−0.62	−0.25	1.9×10^{-4}	0.01264	24.4
SXS:BBH:0209	1.0	−0.90	−0.50	1.7×10^{-4}	0.01137	27.0
SXS:BBH:0226	1.0	+0.50	−0.90	2.4×10^{-4}	0.01340	22.9
SXS:BBH:0286	3.0	+0.50	+0.50	8.0×10^{-5}	0.01693	24.1
SXS:BBH:0253	2.0	+0.50	+0.50	6.7×10^{-5}	0.01397	28.8
SXS:BBH:0267	3.0	−0.50	−0.50	5.6×10^{-5}	0.01410	23.4
SXS:BBH:0218	1.0	−0.50	+0.50	7.8×10^{-5}	0.01217	29.1
SXS:BBH:0238	2.0	−0.50	−0.50	6.9×10^{-5}	0.01126	32.0
SXS:BBH:0288	3.0	+0.60	−0.40	1.9×10^{-4}	0.01729	23.5
SXS:BBH:0287	3.0	+0.60	−0.60	7.0×10^{-5}	0.01684	23.5
SXS:BBH:0283	3.0	+0.30	+0.30	7.6×10^{-5}	0.01646	23.5
SXS:BBH:0282	3.0	+0.30	+0.00	7.5×10^{-5}	0.01629	23.3
SXS:BBH:0281	3.0	+0.30	−0.30	6.7×10^{-5}	0.01618	23.2
SXS:BBH:0277	3.0	+0.00	+0.30	7.0×10^{-5}	0.01595	22.9
SXS:BBH:0284	3.0	+0.40	−0.60	1.5×10^{-4}	0.01656	22.8
SXS:BBH:0278	3.0	+0.00	+0.60	2.1×10^{-4}	0.01623	22.8
SXS:BBH:0256	2.0	+0.60	+0.60	1.0×10^{1}	0.01598	23.9
SXS:BBH:0230	1.0	+0.80	+0.80	1.3×10^{-4}	0.01542	24.2
SXS:BBH:0255	2.0	+0.60	+0.00	4.0×10^{-5}	0.01580	23.3
SXS:BBH:0276	3.0	+0.00	−0.30	6.7×10^{-5}	0.01559	23.0
SXS:BBH:0251	2.0	+0.30	+0.30	7.5×10^{-5}	0.01514	23.5
SXS:BBH:0250	2.0	+0.30	+0.00	7.5×10^{-5}	0.01503	23.2
SXS:BBH:0271	3.0	−0.30	+0.00	6.3×10^{-5}	0.01508	22.5
SXS:BBH:0249	2.0	+0.30	−0.30	7.2×10^{-5}	0.01478	23.2
SXS:BBH:0275	3.0	+0.00	−0.60	1.2×10^{-4}	0.01569	22.6
SXS:BBH:0254	2.0	+0.60	−0.60	6.0×10^{-5}	0.01541	22.9
SXS:BBH:0269	3.0	−0.40	+0.60	1.2×10^{-4}	0.01563	22.3
SXS:BBH:0225	1.0	+0.40	+0.80	3.5×10^{-4}	0.01536	23.5

(Table continued)

(Continued)

ID	q	χ_1	χ_2	e	$M\omega_{22}$	$N_{\rm orb}$
SXS:BBH:0270	3.0	−0.30	−0.30	6.2×10^{-5}	0.01482	22.8
SXS:BBH:0245	2.0	+0.00	−0.30	6.8×10^{-5}	0.01441	23.0
SXS:BBH:0242	2.0	−0.30	+0.30	6.7×10^{-5}	0.01417	23.1
SXS:BBH:0223	1.0	+0.30	+0.00	6.7×10^{-5}	0.01402	23.3
SXS:BBH:0241	2.0	−0.30	+0.00	6.6×10^{-5}	0.01394	23.1
SXS:BBH:0240	2.0	−0.30	−0.30	6.4×10^{-5}	0.01359	23.5
SXS:BBH:0222	1.0	−0.30	+0.00	7.4×10^{-5}	0.01324	23.6
SXS:BBH:0228	1.0	+0.60	+0.60	3.2×10^{-4}	0.01543	23.5
SXS:BBH:0247	2.0	+0.00	+0.60	1.0×10^{-4}	0.01530	22.6
SXS:BBH:0263	3.0	−0.60	+0.60	1.9×10^{-4}	0.01526	22.0
SXS:BBH:0266	3.0	−0.60	+0.40	1.8×10^{-4}	0.01488	22.0
SXS:BBH:0227	1.0	+0.60	+0.00	3.1×10^{-4}	0.01452	23.1
SXS:BBH:0221	1.0	−0.40	+0.80	2.7×10^{-4}	0.01440	22.7
SXS:BBH:0237	2.0	−0.60	+0.60	6.1×10^{-5}	0.01433	22.6
SXS:BBH:0244	2.0	+0.00	−0.60	7.5×10^{-5}	0.01422	23.2
SXS:BBH:0217	1.0	−0.60	+0.60	1.5×10^{-4}	0.01421	22.7
SXS:BBH:0215	1.0	−0.60	−0.60	1.8×10^{-4}	0.01189	25.8
SXS:BBH:0262	3.0	−0.60	+0.00	2.0×10^{-4}	0.01473	22.5
SXS:BBH:0213	1.0	−0.80	+0.80	1.4×10^{-4}	0.01435	22.3
SXS:BBH:0265	3.0	−0.60	−0.40	9.0×10^{-5}	0.01422	23.4
SXS:BBH:0264	3.0	−0.60	−0.60	2.8×10^{-4}	0.01410	23.4
SXS:BBH:0224	1.0	+0.40	−0.80	2.5×10^{-4}	0.01361	22.9
SXS:BBH:0236	2.0	−0.60	+0.00	1.2×10^{-4}	0.01361	23.4
SXS:BBH:0216	1.0	−0.60	+0.00	2.6×10^{-4}	0.01300	23.6
SXS:BBH:0235	2.0	−0.60	−0.60	1.0×10^{1}	0.01274	25.1
SXS:BBH:0220	1.0	−0.40	−0.80	1.0×10^{-4}	0.01195	25.7
SXS:BBH:0212	1.0	−0.80	−0.80	2.4×10^{-4}	0.01087	28.6
SXS:BBH:0303	10.0	+0.00	+0.00	5.1×10^{-5}	0.02395	19.3
SXS:BBH:0300	8.5	+0.00	+0.00	5.7×10^{-5}	0.02311	18.7
SXS:BBH:0299	7.5	+0.00	+0.00	5.9×10^{-5}	0.02152	20.1
SXS:BBH:0298	7.0	+0.00	+0.00	6.1×10^{-5}	0.02130	19.7
SXS:BBH:0297	6.5	+0.00	+0.00	6.4×10^{-5}	0.02082	19.7
SXS:BBH:0296	5.5	+0.00	+0.00	5.2×10^{-5}	0.01668	27.9
SXS:BBH:0295	4.5	+0.00	+0.00	5.2×10^{-5}	0.01577	27.8
SXS:BBH:0259	2.5	+0.00	+0.00	5.9×10^{-5}	0.01346	28.6
SXS:BBH:0292	3.0	+0.73	−0.85	1.8×10^{-4}	0.01749	23.9
SXS:BBH:0268	3.0	−0.40	−0.60	1.7×10^{-4}	0.01473	22.9
SXS:BBH:0234	2.0	−0.85	−0.85	1.4×10^{-4}	0.01147	27.8
SXS:BBH:0273	3.0	−0.27	−0.85	2.0×10^{-4}	0.01487	22.9
SXS:BBH:0210	1.0	−0.90	+0.00	1.8×10^{-4}	0.01248	24.3
SXS:BBH:0260	3.0	−0.85	−0.85	3.5×10^{-4}	0.01285	25.8
SXS:BBH:0302	9.5	+0.00	+0.00	6.0×10^{-5}	0.02366	19.1
SXS:BBH:0301	9.0	+0.00	+0.00	5.5×10^{-5}	0.02338	18.9
SXS:BBH:0272	3.0	−0.30	+0.30	6.4×10^{-5}	0.01521	22.7
SXS:BBH:0246	2.0	+0.00	+0.30	7.2×10^{-5}	0.01514	22.9

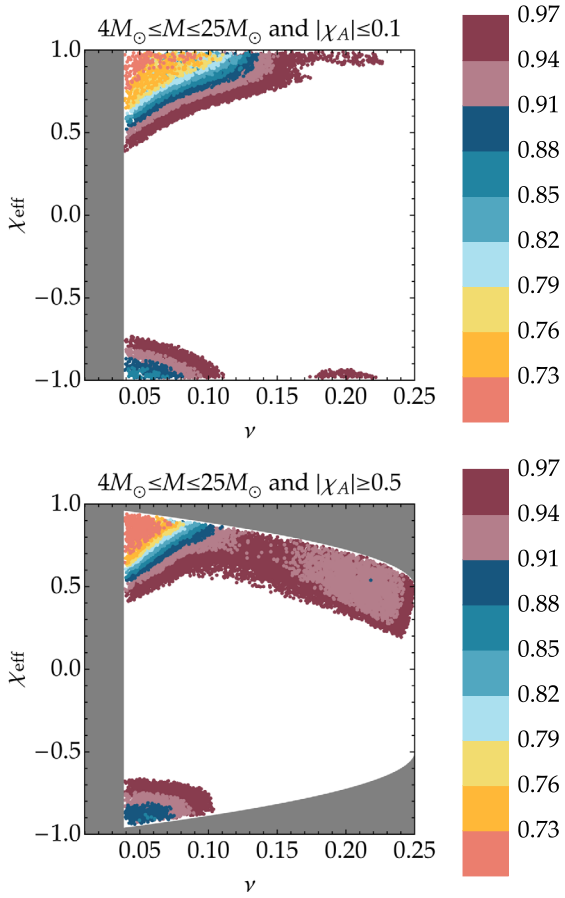

FIG. 13. Faithfulness of the EOBNR model of this paper (SEOBNRv4) against the phenomenological inspiral-merger-ringdown model (IMRPHENOMD) [34] for 10^6 random spinning, nonprecessing BBHs with $4\ M_\odot \leq M \leq 25\ M_\odot$ using the Advanced LIGO O1 noise PSD and a low-frequency cutoff of 25 Hz. When plotting, we restrict the data in $\chi_{\rm A}$ according to the values specified above each plot. Points with faithfulness above 97% are not shown. Note that only 0.9% (2.5%) of points have faithfulness below 97% when $|\chi_{\rm A}| \leq 0.1$ ($|\chi_{\rm A}| \geq 0.5$). Points with faithfulness $\leq 73\%$ are in red.

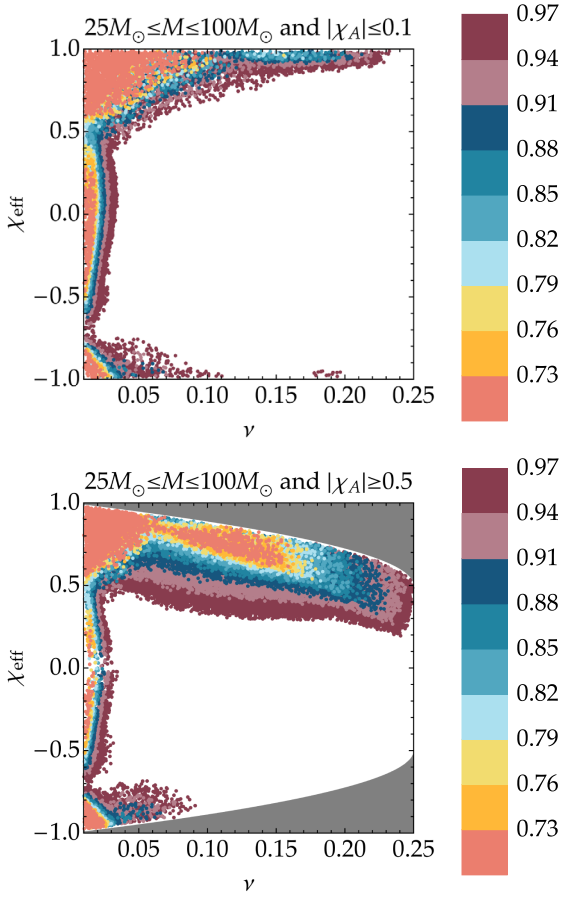

FIG. 14. Same as Fig. 13, but now for BBHs with $25\ M_\odot \leq M \leq 100\ M_\odot$. Note that only 1.1% (5.1%) of points have faithfulness below 97% when $|\chi_{\rm A}| \leq 0.1$ ($|\chi_{\rm A}| \geq 0.5$).

4. BAM waveform from Ref. [34]

ID	q	χ_1	χ_2	e	$M\omega_{22}$	$N_{\rm orb}$
BAMq8s85s85	8.0	+0.85	+0.85	9.1×10^{-3}	0.05476	7.9

APPENDIX D: FAITHFULNESS OF SEOBNRv4 AGAINST IMRPHENOMD

In this Appendix we present faithfulness comparisons between the EOBNR model of this paper (SEOBNRv4) and the phenomenological inspiral-merger-ringdown model (IMRPHENOMD) [34] for specific ranges of total masses and $\chi_{\rm A}$, in order to gain more insight into the plots of Fig. 5, where instead all possible values of these parameters are put together. All plots in this Appendix use the O1 PSD and the same color coding of Fig. 5, namely: (i) points with faithfulness above 97% are white, (ii) points with faithfulness below 73% are red, and (iii) all remaining points are colored according to the legend on the right. We consider three sets of BBHs, each containing 10^6 points. Spins are uniformly sampled in $-0.99 \leq \chi_{1,2} \leq 0.99$. Component masses are uniformly sampled in: (i) $1\ M_\odot \leq M \leq 25\ M_\odot$, subject to the constraint $4\ M_\odot \leq M \leq 25\ M_\odot$, for the first set; (ii) $1\ M_\odot \leq M \leq 100\ M_\odot$, subject to the constraint $25\ M_\odot \leq M \leq 100\ M_\odot$, for the second set; (iii) $1\ M_\odot \leq M \leq 200\ M_\odot$, subject to the constraint $100\ M_\odot \leq M \leq 200\ M_\odot$, for the third set. For each set of BBHs, we split the data into configurations with $|\chi_{\rm A}| \leq 0.1$ and those with $|\chi_{\rm A}| \geq 0.5$. Regions of the $(\nu, \chi_{\rm eff})$ plane that are excluded by the constraints in M or $\chi_{\rm A}$ are shaded in grey.

In Fig. 13 we show results for the first set of BBHs, i.e., those with $4\ M_\odot \leq M \leq 25\ M_\odot$. This low-mass range emphasizes the role of the inspiral in the computation of the matches. We notice that points with faithfulness below 90% are confined to mass ratios above ~5 and $|\chi_{\rm eff}| \gtrsim 0.5$, irrespective of $\chi_{\rm A}$, that is in those regions where the signal spans many GW cycles and where existing NR simulations do not provide strong constraints on models. On the other

hand, it is reassuring that at $q \lesssim 5$ and small values of $|\chi_A|$ the differences in the low-frequency portion of the models are always within 10%. At large values of $|\chi_A|$, differences up to 10% can be found also in the comparable-mass regime.

In Fig. 14 we show results for the second set of BBHs, i.e., those with $25\,M_\odot \leq M \leq 100\,M_\odot$. In this intermediate-mass range both the inspiral and the merger-ringdown contribute to the matches. At mass ratios above ~8, unsurprisingly, we find many points with very poor faithfulness (below 80%). For both approximants, this is the region of extrapolation away from the respective domains of calibration. At smaller mass ratios, whenever $|\chi_A|$ is small (top panel), the faithfulness is good, as long as $\chi_{\rm eff}$ does not exceed ~0.9. However, when $|\chi_A|$ is large (bottom panel), large differences are found even for comparable masses and moderate values of $\chi_{\rm eff}$. This indicates that calibration to NR simulations is not constraining even at these values of total mass. For large $|\chi_A|$'s, even at small mass ratios, large unfaithfulness regions are present. This is expected because of the poorer coverage of the χ_A dimension with NR runs that entered the IMRPhenomD calibration.

Finally, in Fig. 15 we show results for the third set of BBHs, i.e., those with $100\,M_\odot \leq M \leq 200\,M_\odot$. This high-mass range emphasizes the role of the late inspiral and of the merger-ringdown in the computation of the matches. Here we observe distinct behaviors according to the range of χ_A that one considers. For small values of $|\chi_A|$ (top panel), most of the $(\nu, \chi_{\rm eff})$ plane has faithfulness above 97% thanks to the fact that this is precisely the domain that is best constrained by existing NR simulations. In particular, we observe that the white region amply encompasses the location of the most extreme NR waveform that was included in the calibration of SEOBNRv4, i.e., the BAM run at $(q, \chi_1, \chi_2) = (8, 0.85, 0.85)$. At very large mass ratios, very large differences between the models persist. For large values of $|\chi_A|$ (bottom panel), besides the difference at very large mass ratios, we observe many points with faithfulness below 90% for mass ratios as small as 3, for the same reason mentioned above when discussing the intermediate-total-mass set with large $|\chi_A|$'s.

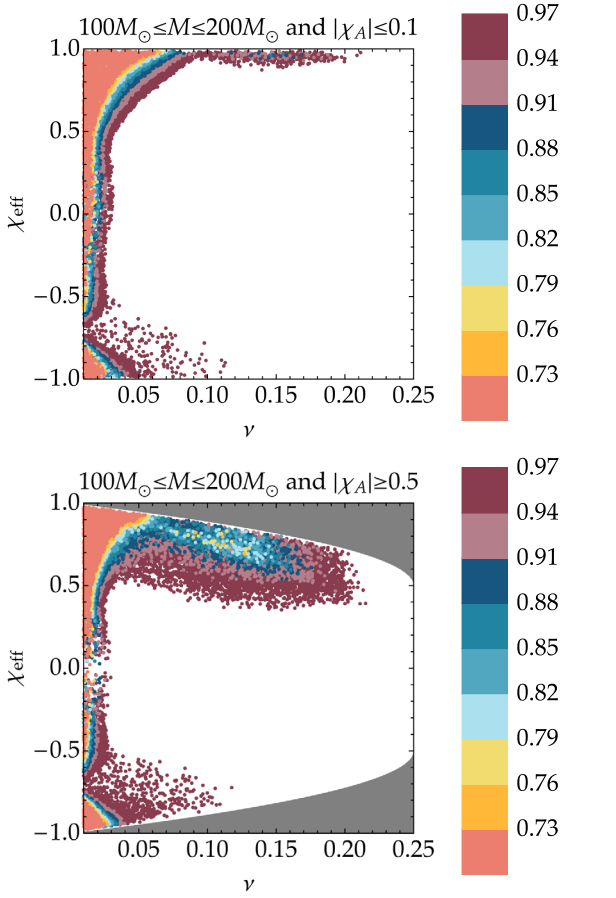

FIG. 15. Same as Fig. 13, but now for BBHs with $100\,M_\odot \leq M \leq 200\,M_\odot$. Note that only 0.9% (2.2%) of points have faithfulness below 97% when $|\chi_A| \leq 0.1$ ($|\chi_A| \geq 0.5$).

[1] B. P. Abbott *et al.* (Virgo and LIGO Scientific Collaboration), Phys. Rev. Lett. **116**, 061102 (2016).
[2] B. P. Abbott *et al.* (Virgo and LIGO Scientific Collaboration), Phys. Rev. Lett. **116**, 241103 (2016).
[3] B. P. Abbott *et al.* (Virgo and LIGO Scientific Collaboration), Phys. Rev. X **6**, 041015 (2016).
[4] B. P. Abbott *et al.* (Virgo and LIGO Scientific Collaboration), Phys. Rev. D **93**, 122004 (2016); **94**, 069903 (2016).
[5] B. P. Abbott *et al.* (Virgo and LIGO Scientific Collaboration), Phys. Rev. D **93**, 122003 (2016).
[6] C. Capano, I. Harry, S. Privitera, and A. Buonanno, Phys. Rev. D **93**, 124007 (2016).
[7] A. Taracchini *et al.*, Phys. Rev. D **89**, 061502 (2014).
[8] M. Pürrer, Phys. Rev. D **93**, 064041 (2016).
[9] A. Buonanno and T. Damour, Phys. Rev. D **59**, 084006 (1999).
[10] A. Buonanno and T. Damour, Phys. Rev. D **62**, 064015 (2000).
[11] T. Damour, P. Jaranowski, and G. Schäfer, Phys. Rev. D **62**, 084011 (2000).
[12] T. Damour, Phys. Rev. D **64**, 124013 (2001).
[13] A. Buonanno, Y. Chen, and T. Damour, Phys. Rev. D **74**, 104005 (2006).
[14] T. Damour, P. Jaranowski, and G. Schäfer, Phys. Rev. D **78**, 024009 (2008).

[15] T. Damour, B. R. Iyer, and A. Nagar, Phys. Rev. D **79**, 064004 (2009).
[16] T. Damour and A. Nagar, Phys. Rev. D **79**, 081503 (2009).
[17] E. Barausse, E. Racine, and A. Buonanno, Phys. Rev. D **80**, 104025 (2009); **85**, 069904 (2012).
[18] E. Barausse and A. Buonanno, Phys. Rev. D **81**, 084024 (2010).
[19] Y. Pan, A. Buonanno, R. Fujita, E. Racine, and H. Tagoshi, Phys. Rev. D **83**, 064003 (2011); **87**, 109901 (2013).
[20] E. Barausse, A. Buonanno, and A. Le Tiec, Phys. Rev. D **85**, 064010 (2012).
[21] T. Damour, A. Nagar, and S. Bernuzzi, Phys. Rev. D **87**, 084035 (2013).
[22] Y. Pan, A. Buonanno, M. Boyle, L. T. Buchman, L. E. Kidder, H. P. Pfeiffer, and M. A. Scheel, Phys. Rev. D **84**, 124052 (2011).
[23] Y. Pan, A. Buonanno, A. Taracchini, L. E. Kidder, A. H. Mroué, H. P. Pfeiffer, M. A. Scheel, and B. Szilágyi, Phys. Rev. D **89**, 084006 (2014).
[24] A. Nagar, T. Damour, C. Reisswig, and D. Pollney, Phys. Rev. D **93**, 044046 (2016).
[25] D. Bini and T. Damour, Phys. Rev. D **93**, 104040 (2016).
[26] S. Babak, A. Taracchini, and A. Buonanno, arXiv:1607.05661.
[27] B. Abbott *et al.* (LIGO Scientific Collaboration), Phys. Rev. D **73**, 062001 (2006).
[28] B. P. Abbott *et al.* (Virgo and LIGO Scientific Collaboration), Phys. Rev. Lett. **116**, 241102 (2016).
[29] B. P. Abbott *et al.* (Virgo and LIGO Scientific Collaboration), Phys. Rev. X **6**, 041014 (2016).
[30] B. P. Abbott *et al.* (Virgo and LIGO Scientific Collaboration), Phys. Rev. Lett. **116**, 221101 (2016).
[31] Y. Pan, A. Buonanno, J. G. Baker, J. Centrella, B. J. Kelly, S. T. McWilliams, F. Pretorius, and J. R. van Meter, Phys. Rev. D **77**, 024014 (2008).
[32] P. Ajith *et al.*, Phys. Rev. D **77**, 104017 (2008); **79**, 129901(E) (2009).
[33] M. Hannam, P. Schmidt, A. Bohe, L. Haegel, S. Husa, F. Ohme, G. Pratten, and M. Purrer, Phys. Rev. Lett. **113**, 151101 (2014).
[34] S. Khan, S. Husa, M. Hannam, F. Ohme, M. Pürrer, X. Jiménez Forteza, and A. Bohé, Phys. Rev. D **93**, 044007 (2016).
[35] P. Kumar, T. Chu, H. Fong, H. P. Pfeiffer, M. Boyle, D. A. Hemberger, L. E. Kidder, M. A. Scheel, and B. Szilagyi, Phys. Rev. D **93**, 104050 (2016).
[36] https://www.lsc-group.phys.uwm.edu/daswg/projects/lalsuite.html.
[37] L. Blanchet, Living Rev. Relativ. **17**, 2 (2014).
[38] A. H. Mroue *et al.*, Phys. Rev. Lett. **111**, 241104 (2013).
[39] T. Chu, H. Fong, P. Kumar, H. P. Pfeiffer, M. Boyle, D. A. Hemberger, L. E. Kidder, M. A. Scheel, and B. Szilagyi, Classical Quantum Gravity **33**, 165001 (2016).
[40] G. Lovelace, M. Scheel, and B. Szilagyi, Phys. Rev. D **83**, 024010 (2011).
[41] M. A. Scheel, M. Giesler, D. A. Hemberger, G. Lovelace, K. Kuper, M. Boyle, B. Szilágyi, and L. E. Kidder, Classical Quantum Gravity **32**, 105009 (2015).
[42] S. Husa, S. Khan, M. Hannam, M. Pürrer, F. Ohme, X. Jiménez Forteza, and A. Bohé, Phys. Rev. D **93**, 044006 (2016).
[43] B. Szilágyi, J. Blackman, A. Buonanno, A. Taracchini, H. P. Pfeiffer, M. A. Scheel, T. Chu, L. E. Kidder, and Y. Pan, Phys. Rev. Lett. **115**, 031102 (2015).
[44] A. Nagar, T. Damour, C. Reisswig, and D. Pollney, Phys. Rev. D **93**, 044046 (2016).
[45] A. Taracchini, Y. Pan, A. Buonanno, E. Barausse, M. Boyle, T. Chu, G. Lovelace, H. P. Pfeiffer, and M. A. Scheel, Phys. Rev. D **86**, 024011 (2012).
[46] E. Barausse and A. Buonanno, Phys. Rev. D **84**, 104027 (2011).
[47] J. Steinhoff, T. Hinderer, A. Buonanno, and A. Taracchini, Phys. Rev. D **94**, 104028 (2016).
[48] D. Bini and T. Damour, Phys. Rev. D **87**, 121501 (2013).
[49] K. G. Arun, A. Buonanno, G. Faye, and E. Ochsner, Phys. Rev. D **79**, 104023 (2009); **84**, 049901(E) (2011).
[50] A. Buonanno, G. Faye, and T. Hinderer, Phys. Rev. D **87**, 044009 (2013).
[51] T. Damour and A. Nagar, Phys. Rev. D **76**, 064028 (2007).
[52] T. Damour and A. Nagar, Phys. Rev. D **90**, 044018 (2014).
[53] L. Blanchet, A. Buonanno, and G. Faye, Phys. Rev. D **84**, 064041 (2011).
[54] A. Bohé, S. Marsat, and L. Blanchet, Classical Quantum Gravity **30**, 135009 (2013).
[55] Y. Pan, A. Buonanno, L. T. Buchman, T. Chu, L. E. Kidder, H. P. Pfeiffer, and M. A. Scheel, Phys. Rev. D **81**, 084041 (2010).
[56] E. Barausse, A. Buonanno, S. A. Hughes, G. Khanna, S. O'Sullivan, and Y. Pan, Phys. Rev. D **85**, 024046 (2012).
[57] A. Taracchini, A. Buonanno, G. Khanna, and S. A. Hughes, Phys. Rev. D **90**, 084025 (2014).
[58] R. H. Price and G. Khanna, Phys. Rev. D **94**, 104026 (2016).
[59] J. G. Baker, W. D. Boggs, J. Centrella, B. J. Kelly, S. T. McWilliams, and J. R. van Meter, Phys. Rev. D **78**, 044046 (2008).
[60] T. Damour and A. Nagar, Phys. Rev. D **90**, 024054 (2014).
[61] A. Nagar and W. Del Pozzo, arXiv:1606.03952.
[62] E. Berti, V. Cardoso, and C. M. Will, Phys. Rev. D **73**, 064030 (2006).
[63] E. Barausse, V. Morozova, and L. Rezzolla, Astrophys. J. **758**, 63 (2012); **786**, 76(E) (2014).
[64] D. A. Hemberger, G. Lovelace, T. J. Loredo, L. E. Kidder, M. A. Scheel, B. Szilágyi, N. W. Taylor, and S. A. Teukolsky, Phys. Rev. D **88**, 064014 (2013).
[65] F. Hofmann, E. Barausse, and L. Rezzolla, Astrophys. J. **825**, L19 (2016).
[66] P. Kumar, K. Barkett, S. Bhagwat, N. Afshari, D. A. Brown, G. Lovelace, M. A. Scheel, and B. Szilágyi, Phys. Rev. D **92**, 102001 (2015).
[67] http://www.black-holes.org/SpEC.html.
[68] M. A. Scheel, H. P. Pfeiffer, L. Lindblom, L. E. Kidder, O. Rinne, and S. A. Teukolsky, Phys. Rev. D **74**, 104006 (2006).
[69] B. Szilagyi, L. Lindblom, and M. A. Scheel, Phys. Rev. D **80**, 124010 (2009).
[70] L. T. Buchman, H. P. Pfeiffer, M. A. Scheel, and B. Szilagyi, Phys. Rev. D **86**, 084033 (2012).
[71] L. Lindblom, M. A. Scheel, L. E. Kidder, R. Owen, and O. Rinne, Classical Quantum Gravity **23**, S447 (2006).
[72] H. Friedrich, Commun. Math. Phys. **100**, 525 (1985).

[73] F. Pretorius, Phys. Rev. Lett. **95**, 121101 (2005).
[74] L. Lindblom and B. Szilagyi, Phys. Rev. D **80**, 084019 (2009).
[75] D. A. Hemberger, M. A. Scheel, L. E. Kidder, B. Szilágyi, G. Lovelace, N. W. Taylor, and S. A. Teukolsky, Classical Quantum Gravity **30**, 115001 (2013).
[76] B. Szilágyi, Int. J. Mod. Phys. D **23**, 1430014 (2014).
[77] M. Boyle and A. H. Mroue, Phys. Rev. D **80**, 124045 (2009).
[78] F. Loffler *et al.*, Classical Quantum Gravity **29**, 115001 (2012).
[79] T. Goodale, G. Allen, G. Lanfermann, J. Massó, T. Radke, E. Seidel, and J. Shalf, in *Vector and Parallel Processing—VECPAR'2002, 5th International Conference, Lecture Notes in Computer Science* (Springer, Berlin, 2003).
[80] J. M. Bowen and J. W. York, Phys. Rev. D **21**, 2047 (1980).
[81] S. Brandt and B. Brügmann, Phys. Rev. Lett. **78**, 3606 (1997).
[82] M. Ansorg, B. Bruegmann, and W. Tichy, Phys. Rev. D **70**, 064011 (2004).
[83] H. P. Pfeiffer, D. A. Brown, L. E. Kidder, L. Lindblom, G. Lovelace, and M. A. Scheel, Classical Quantum Gravity **24**, S59 (2007).
[84] T. Nakamura, K. Oohara, and Y. Kojima, Prog. Theor. Phys. Suppl. **90**, 1 (1987).
[85] M. Shibata and T. Nakamura, Phys. Rev. D **52**, 5428 (1995).
[86] T. W. Baumgarte and S. L. Shapiro, Phys. Rev. D **59**, 024007 (1998).
[87] J. D. Brown, P. Diener, O. Sarbach, E. Schnetter, and M. Tiglio, Phys. Rev. D **79**, 044023 (2009).
[88] J. G. Baker, J. Centrella, D.-I. Choi, M. Koppitz, and J. van Meter, Phys. Rev. Lett. **96**, 111102 (2006).
[89] M. Campanelli, C. Lousto, P. Marronetti, and Y. Zlochower, Phys. Rev. Lett. **96**, 111101 (2006).
[90] E. Schnetter, S. H. Hawley, and I. Hawke, Classical Quantum Gravity **21**, 1465 (2004).
[91] D. Pollney, C. Reisswig, E. Schnetter, N. Dorband, and P. Diener, Phys. Rev. D **83**, 044045 (2011).
[92] J. Thornburg, Classical Quantum Gravity **21**, 743 (2004).
[93] O. Dreyer, B. Krishnan, D. Shoemaker, and E. Schnetter, Phys. Rev. D **67**, 024018 (2003).
[94] C. Reisswig and D. Pollney, Classical Quantum Gravity **28**, 195015 (2011).
[95] S. Husa, I. Hinder, and C. Lechner, Comput. Phys. Commun. **174**, 983 (2006).
[96] M. Thomas and E. Schnetter, in *Grid Computing (GRID), 2010 11th IEEE/ACM International Conference on* (IEEE, 2010), pp. 369–378.
[97] B. Wardell, I. Hinder, and E. Bentivegna, Simulation of GW150914 binary black hole merger using the Einstein Toolkit, 2016.
[98] I. Hinder and B. Wardell, SimulationTools for Mathematica, http://simulationtools.org.
[99] B. Bruegmann, J. A. Gonzalez, M. Hannam, S. Husa, U. Sperhake, and W. Tichy, Phys. Rev. D **77**, 024027 (2008).
[100] S. Husa, J. A. Gonzalez, M. Hannam, B. Bruegmann, and U. Sperhake, Classical Quantum Gravity **25**, 105006 (2008).
[101] T. Regge and J. A. Wheeler, Phys. Rev. **108**, 1063 (1957).
[102] F. J. Zerilli, J. Math. Phys. **11**, 2203 (1970).
[103] S. A. Teukolsky, Astrophys. J. **185**, 635 (1973).
[104] S. Bernuzzi, A. Nagar, and A. Zenginoglu, Phys. Rev. D **83**, 064010 (2011).
[105] L. Lindblom, Phys. Rev. D **80**, 064019 (2009).
[106] L. Lindblom, J. G. Baker, and B. J. Owen, Phys. Rev. D **82**, 084020 (2010).
[107] T. B. Littenberg, J. G. Baker, A. Buonanno, and B. J. Kelly, Phys. Rev. D **87**, 104003 (2013).
[108] L. S. Finn, Phys. Rev. D **46**, 5236 (1992).
[109] D. Shoemaker (LIGO Collaboration), Advanced LIGO anticipated sensitivity curves, LIGO Document No. T0900288-v3, 2010.
[110] D. J. A. McKechan, C. Robinson, and B. S. Sathyaprakash, Classical Quantum Gravity **27**, 084020 (2010).
[111] D. J. C. Mackay, *Information Theory, Inference and Learning Algorithms* (Cambridge University Press, Cambridge, England, 2003).
[112] D. Foreman-Mackey, D. W. Hogg, D. Lang, and J. Goodman, Publ. Astron. Soc. Pac. **125**, 306 (2013).
[113] J. Goodman and J. Weare, Commun. Appl. Math. Comput. Sci., **5** 65 (2010).
[114] S. Brooks, A. Gelman, G. Jones, and X. Meng, *Handbook of Markov Chain Monte Carlo*, Chapman & Hall/CRC Handbooks of Modern Statistical Methods (CRC Press, London, 2011).
[115] J. A. Nelder and R. Mead, Computer Journal (UK) **7**, 308 (1965).
[116] D. V. Martynov *et al.* (LIGO Scientific Collaboration), Phys. Rev. D **93**, 112004 (2016).
[117] M. Pürrer, Classical Quantum Gravity **31**, 195010 (2014).
[118] R. Smith, K. Cannon, C. Hanna, D. Keppel, and I. Mandel, Phys. Rev. D **87**, 122002 (2013).
[119] K. Cannon, J. Emberson, C. Hanna, D. Keppel, and H. Pfeiffer, Phys. Rev. D **87**, 044008 (2013).
[120] K. Cannon, C. Hanna, and D. Keppel, Phys. Rev. D **85**, 081504 (2012).
[121] S. E. Field, C. R. Galley, J. S. Hesthaven, J. Kaye, and M. Tiglio, Phys. Rev. X **4**, 031006 (2014).
[122] S. E. Field, C. R. Galley, F. Herrmann, J. S. Hesthaven, E. Ochsner, and M. Tiglio, Phys. Rev. Lett. **106**, 221102 (2011).
[123] J. Blackman, B. Szilagyi, C. R. Galley, and M. Tiglio, Phys. Rev. Lett. **113**, 021101 (2014).
[124] J. Blackman, S. E. Field, C. R. Galley, B. Szilágyi, M. A. Scheel, M. Tiglio, and D. A. Hemberger, Phys. Rev. Lett. **115**, 121102 (2015).
[125] C. Devine, Z. B. Etienne, and S. T. McWilliams, Classical Quantum Gravity **33**, 125025 (2016).
[126] C. Capano, Y. Pan, and A. Buonanno, Phys. Rev. D **89**, 102003 (2014).
[127] I. MacDonald, S. Nissanke, and H. P. Pfeiffer, Classical Quantum Gravity **28**, 134002 (2011).
[128] F. Ohme, M. Hannam, and S. Husa, Phys. Rev. D **84**, 064029 (2011).
[129] Y. Pan, A. Buonanno, A. Taracchini, M. Boyle, L. E. Kidder, A. H. Mroue, H. P. Pfeiffer, M. A. Scheel, B. Szilagyi, and A. Zenginoglu, Phys. Rev. D **89**, 061501 (2014).
[130] A. Nagar (private communication).